IMPERIAL COLLEGE LONDON

Faculty of Engineering

Department of Civil and Environmental Engineering

Investigation into Web Optimisation for Slender I Sections in Major Axis Buckling

Wenxuan Hong

2021-2022

Submitted in fulfilment of the requirements for the MSc and the Diploma of Imperial College London

DECLARATION OF OWN WORK

Declaration:

This submission is my own work. Any quotation from, or description of, the work of others is acknowledged herein by reference to the sources, whether published or unpublished.

Signature : Wenxuan Hong

Imperial College London

Abstract

In the past two decades, additive manufacturing (AM), or 3D printing, has gained popularity in multiple industries and academia, offering a great opportunity to build parts with complex geometry or varying material properties. The possibility of structure optimisation with varying cross-sections and demand-oriented opening patterns is presented, benefiting from the flexibility of additive manufacturing. However, the studies and applications of structural optimisation in this manner are limited at present, constrained by the traditional manufacturing techniques.

The design and assessment of thin-walled steel I-shaped columns with varying cross-sections and different opening patterns were carried out in this research. The concept of optimisation is removing the material from the less stressed region and redistributing it to locations with high stress levels. A series of parametric studies concerning manually made constant height ratio web opening and tapered web opening were performed in ABAQUS, where four parameters were involved, including opening length, opening height, spacing and width of cross-bracings. Moreover, the topology optimisations with different volume constraints and penalty factors were performed, in which the capability of nonlinear topology optimisation in improving the structural performance was investigated.

For models with constant height ratio opening and tapered opening, a 4.1% and 3.2% drop in column resistance were observed in comparison of the benchmark column, respectively. The normalised resistance from columns in topology optimisation resulted in a 27.8% reduction, according to which the significance of local buckling should be taken into account in the optimisation of structural members with openings, and relevant research will continue in the future.

Keywords:

Additive manufacturing; Wire and arc additive manufactured steel; Finite element modelling; Parametric studies; Web opening configuration; Nonlinear topology optimisation

Imperial College London

Acknowledgements

I would like to express my sincere gratitude to many people who have assisted me in preparation of this dissertation, helped and accompanied me during my MSc programme at Imperial College London.

- First and foremost, my genuine thanks to my supervisor Prof. Leroy Gardner, who provided with me endless help and imparted to me the valuable knowledge. With his patient guidance, I was able to complete this individual research project and step further in my research life;

- My sincere thanks to Ben Weber for his valuable guidance. His guidance concerning nonlinear topology optimisation modelling in ABAQUS facilitated my understandings and enhanced my finite element modelling skills which is of great help in this project.

- My sincere thanks to Omer Ayhan and my friends, with whom we collaborate and overcome the difficulties together. From whom I got a lots of supports and inspirations;

- My warm thanks to my girl friend Sitian Deng, who accompanied me through joys and hardships during my MSc programme in UK. Though we lived in different cities, she always encouraged me to overcome the obstacles in life and inspired me with her optimism;

- Last but not least, my special thanks to my family, who offered me unconditional help, support and care during my MSc study.

Table of Contents

List of Tables

List of Figures

List of Notations

A_{min}	Minimum cross-section area
a_{amp}	Web amplitude of the reference column
a_{mod}	Modified web amplitude for consistent volume
E	Young's modulus of WAAM S550 carbon steel
$e_{0,d}$	Global imperfection
f_y	Yielding strength of WAAM S550 carbon steel
H	Width of the column in the middle
H_{hole}	Height of the opening in the middle
H_{in}	Initial height at column ends (centreline dimension)
L	Total length of the column
L_{cr}	Critical buckling length
L_{hole}	Length of opening
$N_{cr,g}$	Eigenvalue of lowest global buckling mode from LBA
$N_{cr,l}$	Eigenvalue of lowest local buckling mode from LBA
N_{Ed}	Design load
$N_{u,FE}$	Collapse load from FE analysis.
n_{Lr}	Number of lateral restraints
P_{cr}	Critical buckling load
P_{max}	Maximum column resistance
R_{end}	Ratio of tapered opening height to constant ratio height at ends
R_H	Ratio of opening height to the web width of the reference column
R_L	Ratio of opening length to the total column length
S	Spacing of the cross-bracing
t_f	Thickness of flanges
$U_{2,max}$	Maximum transverse displacement perpendicular to flanges

$U_{3,max}$	Maximum displacement perpendicular to web
V_i	Total volume of column
$V_{w,ref}$	Volume of web in the reference column
w	Width of the cross-bracing
ΔV_i	Volume of material removed from web
δ_{ref}	Relative difference in P_{max} between column with opening and the benchmark
ε_{eng}	Engineering strain
ε_{sh}	Strain of strain hardening
ε_{true}	True strain
ε_u	Ultimate strain
ε_y	Yielding strain
$\bar{\lambda}$	Non-dimensional slenderness / Relative slenderness
$\bar{\lambda}_p$	Cross-section slenderness
ρ	Normalised collapse load
σ_{eng}	Engineering stress
σ_{true}	True stress
ω_g	Global imperfection
ω_l	Local imperfection

Imperial College London

List of Abbreviations and Acronyms

AM	Additive manufacturing
CHR	Constant height ratio
DED	Directed energy deposition
DMD	Direct material deposition
EBAM	Electron-beam additive manufacturing
FE	Finite element
GMNIA	Geometrically and materially nonlinear analysis with imperfections
LBA	Linear buckling analysis
LENS	Laser engineered net shaping
PBF	Powder bed fusion
PF	Material interpolation penalty factor
SLS	Selective laser sintering
SLM	Selective laser melting
SIMP	Solid isotropic material with penalisation
TO	Topology optimisation
VF	Volume fraction
WAAM	Wire and arc additive manufacturing
3D	Three-dimensional

Imperial College London

Chapter 1 — Introduction

1.1 Background

Additive manufacturing (AM), also known as 3D printing has gained its popularity in industries and academic fields in the past two decades, since it was formally proposed as photo sculpture in the 1860s (Gao et al., 2015). This technology can be elaborated as the automated process of producing 3D parts by placing the material layer by layer controlled by computer programmes, which offers great opportunities to create objects in complex geometries with varying material properties by changing the material layout and deposing different types of materials (Wong & Hernandez, 2012; Gao et al., 2015).

Attributed to the flexibility in manufacturing process presented by AM, this technology is increasingly applied in many fields, especially aerospace and biomedical engineering (Buchanan & Gardner, 2019). It is noted that most of the products from AM in these two fields are high value end use parts which are relatively small in size and highly customised in accordance with the needs of application (Berman, 2012; Thompson et al., 2016). Furthermore, the AM shows its advantages in architectural and structural engineering as well, where for instance by 3D printing, the material in structures could be placed in specific locations to maximise the structural efficiency and reduce material consumption (Bletzinger & Ramm, 2001; Phair, 2004). Also based on AM, the level of customisation and architectural freedom are improved, making it easier to create structures with varying cross-sections, functionally graded components and irregular openings in structural members, beyond the ability of traditional manufacturing methods (Buchanan & Gardner, 2019). Hence, AM started to be investigated in the construction sector, and many applications were reported comprising some structural components like joints and connections (Strauss et al., 2015), houses, offices (Galjaard et al., 2015; Winsun, 2016) and full size pedestrian bridges (Malik Chua, 2017; Gardner et al., 2020), in which the possibilities of different construction materials including concrete, polymer and metal were explored as well.

As one of the key technologies in the field of additive manufacturing, metal 3D printing attracted much attention in the construction sector, which as a new construction method could lead to solutions with reduced embodied carbon and high resource efficiency (Kanyilmaz et al., 2021). As described in ISO/ASTM 52900, there are three viable methods for metal AM in the construction sector at present, including powder bed fusion (PBF), directed energy deposition (DED) and sheet lamination (ASTM International, 2015). Wire and arc additive manufacturing

(WAAM) is one of the DED techniques that employs a robot arm to build up the object layer by layer with wire and arc welding tools, which allows for high deposition rates and unlimited part sizes. Since WAAM uses standard off-the-shelf equipment, and the wire feedstock is cheaper than metallic powder by an order of magnitude, WAAM offers significant advantages over other metal AM methods in construction, especially metallic powder based printing techniques (Buchanan & Gardner, 2019).

The following research in this dissertation assumes that WAAM will be used as the 3D printing technique to produce the optimised columns.

In terms of column optimisation, the main issues that should be paid attention to are the two column failure phenomena: material failure and buckling which are related to the column non-dimensional slenderness $\bar{\lambda}$ (British Standards Institution, 2005). For stocky columns with a low slenderness value, the yielding failure will dominate the column performance and the axial stress will constitute the majority of the stress in the cross-section. This is due to the large flexural stiffness of the stocky column, for which the buckling induced lateral deformation and secondary bending moment in column under axial compression are not significant, resulting in a relatively small magnitude of bending stress which could be neglected. However, for slender columns, the flexural buckling becomes the major failure mode that dominates the maximum column resistance to axial compression. In this case, the bending stress should be paid attention to, especially at the critical mid-height location for columns with prismatic section. Therefore, the material utilisation for slender columns could be significantly improved, particularly at ends with pinned boundary conditions based upon the stress distribution, in contrast to stocky columns which are utilised more uniformly because of the predominant axial stress in cross-section (Laghi et al., 2020).

Hence, the flexural buckling failure will be focused in this investigation by initially proposing a reference column with a 1500.0 mm length and 40.0 mm for both height and width, whose non-dimensional slenderness $\bar{\lambda}$ is set to 1.5 approximately, ensuring that the elastic buckling failure will occur rather than plastic squashing (Gardner & Nethercot, 2011). The thicknesses for both flanges and web of the reference column with uniform cross-section are 5.0 mm as illustrated in **Figure 1.1** (not to scale).

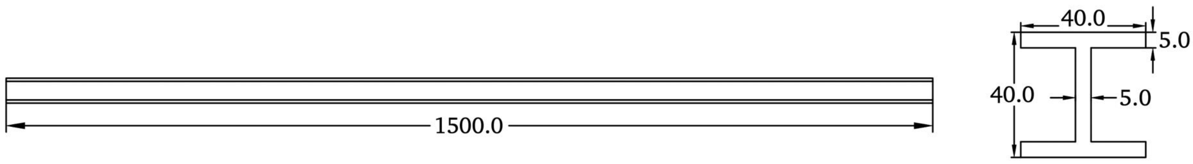

(a) Side view (b) Profile

Figure 1.1: Reference column with uniform cross-section (unit: mm)

It is recommended that columns under compression should have convex cross-sections with tapered ends in order to increase the cross-sectional area and, therefore, the moment of area at the middle (Keller, 1960). WAAM technology enabled the non-prismatic section members to be easily printed, allowing the concept to become a reality for columns with varying cross-sections. Hence, Duque (2022) carried out a study to obtain the maximum resistance by varying the web height according to the first global buckling shape of a pin-ended slender column - a half wave length of a sinusoidal function, and the total volume was kept at 825000 mm^3, as shown in **Figure 1.2**. According to Duque's research, the optimum initial height and amplitude of the sine function are 73.5 mm and 8.3538 mm, and the thickness for flanges and web are 3.5 mm which is the minimum value achieved by the metal 3D printer from MX3D (Gardner et al., 2020).

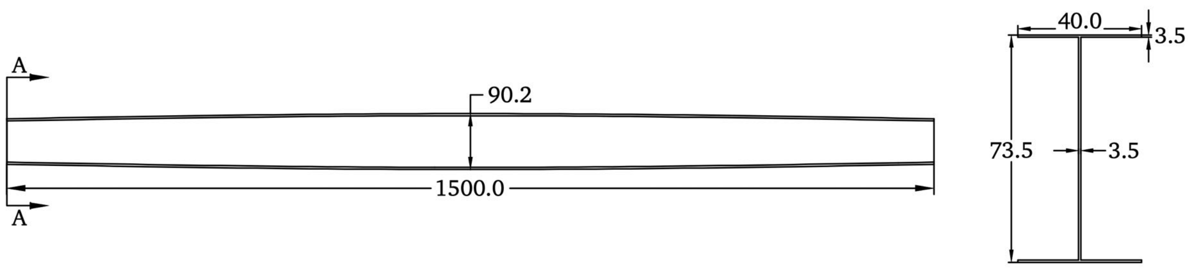

(a) Side view (b) Profile A-A

Figure 1.2: Reference column with varying cross-section (unit: mm)

The purpose of this optimised column against buckling is only to maximise the utilisation ratio of materials in extreme fibres on the outer surface of flanges. While, the materials in the central region near the neutral axis are not effectively utilised, especially for buckling dominated slender columns, since the linearly distributed stress in the cross-section gives zero bending stress at the neutral axis, where only axial stress is counted. Therefore, web openings could be created in the central region along the column length, to remove those less utilised materials and maximise the rest of the web sections connected to flanges.

Many researchers have conducted research concerning the optimisation of structural members with reduced web sections, either by parametric studies or topology optimisation (TO), which will be discussed in detail in the literature review.

1.2 Aim

This research study aims to propose the optimum design of a 3D printed thin-walled steel I-section column, by investigating the effects of creating web openings with cross-bracings in improving column maximum resistance to axial compression from both parametric studies (manually created web opening: ① constant height ratio or ② tapered ends) and nonlinear topology optimisation.

1.3 Objectives

- Verification of finite element (FE) model of the reference column with uniform cross-section built in FE analysis package ABAQUS.
  - Establish the FE model of straight reference column in ABAQUS, and conduct the linear buckling analysis (LBA).
  - Validate the finite element model by attesting the critical buckling load equal to the theoretical value.

- Maximum resistance to axial compression of the reference sinusoidal column.
  - Build the FE model of the column with sinusoidal varying cross-section according to Duque's research using ABAQUS.
  - Perform the LBA and geometrically and materially nonlinear analysis with imperfections (GMNIA) to obtain the load at failure.

- Maximum axial compression resistance and its variation trend for columns with different web opening dimensions (constant height ratio) and cross-bracing widths and spacings.
  - Establish 375 FE models of the column with constant height ratio web opening using ABAQUS and python script.
  - Conduct the LBA and GMNIA in ABAQUS to get corresponding maximum resistance for all 375 FE models.

- Maximum axial compression resistance and its variation trend for columns with different web opening dimensions (tapered ends) and cross-bracing widths and spacings.

  - Build 375 FE models of the column with web opening tapered at ends using ABAQUS and python script.
  - Carry out the LBA and GMNIA in ABAQUS to get the maximum resistance for all 375 columns.

- Verification of the principle that describes how the shape and dimension of opening and pattern of cross-bracing affect the maximum column resistance and failure mode.
  - Compare the outputs of the failure load from the models with different web opening dimensions and cross-bracing patterns.

- Maximum axial compression resistance of columns in topology optimisation with different volume fractions.
  - Establish 70 FE models of the sinusoidal column and conduct topology optimisation using TOSCA embedded in ABAQUS.
  - Perform the LBA and GMNIA to obtain the failure load for all columns from topology optimisation using ABAQUS.

- Optimum column design based on the results of finite element analysis, which has the best performance in resisting the axial compression that can be applied in future engineering practice.

Chapter 2 — Literature Review

2.1 Introduction

In this chapter, the literature review will be presented, mainly focusing on the metal additive manufacturing, structural column optimisation and topology optimisation, where its history and applications will be briefly introduced. Then, based on the review, the limitations of previous research works are analysed, following a summary of the research gap, and significance of this research study.

2.2 Literature review

2.2.1 Additive manufacturing of metal

Over 100 years ago, Blanther (1892) invented the “cut and stack” method for wax plate sheets manufacturing to make the three-dimensional relief-maps with the topographical peculiarities of the locality. This approach was further applied to metal plates by DiMatteo (1976) and Nakagawa et al. (1985) using milling cutter and laser. Except the method of cutting and stacking, the other main technique of metal 3D printing is weld overlay, invented in 1925 by Baker, which aims to use electric arc as heat source and deposit the weld beads layer by layer to create 3D objects, as shown in **Figure 2.1**.

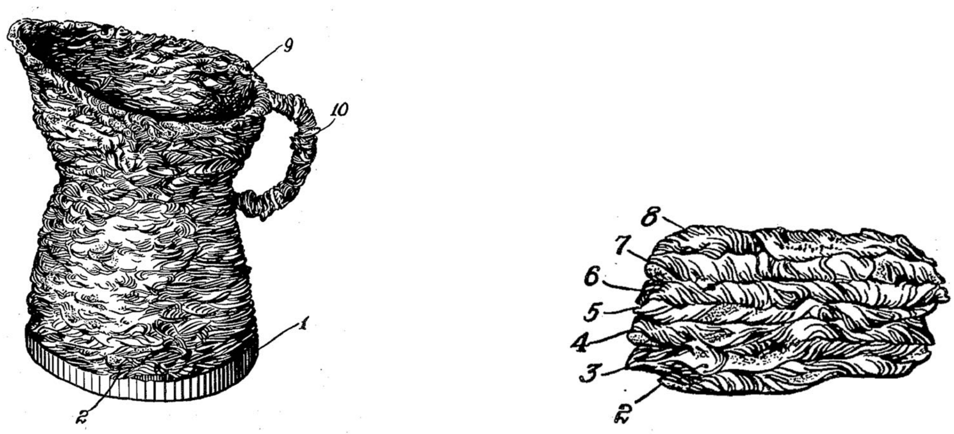

(a) A kettle produced by AM (b) Elevation view of a wall section

Figure 2.1: Weld overlay approach to metal 3D printing (Baker, 1925:p.1)

The modern 3D printing technology is considered to be developed starting in 1987, with the first commercial 3D printer was released (SLA-1) by 3D Systems Corporation, based on when a rapid development of metal 3D printing was observed in the early 1990s, during which time many techniques for metal 3D printing emerged simultaneously, such as PEF and DED, etc.

In 1990, the metal parts printed by the modern AM techniques were firstly reported in the United States. Manriquez-Frayre and Bourell (1990) produced a 7 cm-diameter metal gear by the means of laser sintering of metallic powder which is regarded as a beginning of the researches on direct selective laser sintering (SLS). In 1991, The University of Texas started their researches on SLS and developed the second and third generation of direct SLS in 1995 and 1998 (Moore, 1996; Das, 1998), which was patented by Das and Beaman in 2004. In the same period, the direct metal laser melting was developed in Germany and Belgium since 1991 and the term selective laser melting (SLM) was firstly used by Meiners, which was patented in 2003. These two method are both classified as powder bed fusion technique, which have similar processing methods for consolidation of the metal powder (Das et al., 2016). Compared with laser sintering, the laser melting results in a nearly fully dense structure since the metallic powder is completely melted during heating. Hence, the micro-structural homogeneity is well realised by laser melting, which leads to a better mechanical performance.

The directed energy deposition is another AM technology which creates a melt pool by utilising laser, electron beam or a gas-tungsten arc, etc. as the heat source and place the powder or wire material in the melt pool to form the objects. Based on the different heating sources, the DED could be further classified as wire and arc additive manufacturing (WAAM), direct metal deposition (DMD), laser engineered net shaping (LENS) and electron-beam additive manufacturing (EBAM), etc. The first commercial application of DED in engineering practice was reported in 1997 by Aeromet Corporation, who applied the LENS in manufacturing of the large titanium aerospace components (Dutta, 2022). Among various DED techniques, WAAM offers a relatively low start-up cost by employing off-the-shelf equipment and consumable wire as a filler material that could cover a wide range of materials with different properties. Moreover, the high deposition rate and unlimited parts size make WAAM viable in large-scale metal parts manufacturing, offering an option that combines rapidness and cost-effectiveness. Hence, more and more WAAM applications were reported in different fields to investigate the capabilities of WAAM especially in construction sector, such as the stainless steel bridge and the TAKENAKA steel connector manufactured by MX3D as shown in **Figure 2.2**.

(a) World's first 3D printed stainless steel bridge (Gardner et al., 2020:p.2)

(b) TAKENAKA steel connector (MX3D, 2019)

Figure 2.2: WAAM applications from MX3D

Due to the high level of geometric and material flexibility, WAAM provides the basis for structure optimisation, by which the structures manufactured could comply to the shape that has the maximised performance with minimum material consumption or uniform material utilisation. Topology optimisation is an approach to computationally determine the optimal solution of materials layouts in structural members which can not be easily realised by traditional fabrication method (Buchanan & Gardner, 2019). Therefore, the high degree of customisation of WAAM provides the basis to create flexible structural geometries and opens the possibilities for the topology optimisation solutions to be widely manufactured in practical engineering projects.

2.2.2 Column optimisation against buckling

As mentioned previously, buckling is a common failure mode for slender columns, in which the stress distribution is not uniform, and the materials are not fully utilised in lightly stressed regions. Hence, the space for improvement in material utilisation along the column is potentially very high, focusing on which, there are many studies conducted in the past decades. The majority of them aimed to obtain the strength improvement by changing the shape of the columns, where the eigenvalue optimisation algorithm was applied based on either continuous or finite element models.

The first column optimisation study dates back to 200 years ago, Lagrange (1770) failed to derive the optimal shape for a column, which only obtained the column with greatest buckling load under given length and volume. Then, in 1851, the optimal shape for pinned column with circular cross-section was proposed by Clausen (1851), whose work is replicated and updated by Keller (1960).

In the early 1910s, the minimum weight optimisation was conducted by Blasius (1914) who derived the optimum shape of solid columns based on variational principles which achieved the minimum weight by making the bending stress uniformly distributed along column. Based on the research for solid column, Feigen (1952) focused on the thin-walled cylindrical column and derived its optimal shape, stating that for double truncated cone, the end to middle diameter ratio (D_e/D_m) ranging from 0.35 to 0.5 approaches the optimum column shape. However, both of them did the calculations based on the stress distribution in uniform cross-section column with only elastic material property.

In 1936, Timoshenko firstly discussed the buckling issue of bars with varying cross-section and proposed the buckling coefficient for some bars with certain cross-sections and taper ratios (Timoshenko, 1936), which is further developed by Gatewood (1954) who presented the buckling coefficient curves covering the columns with all taper ratios and cross-sections with second moment of area variation between constant and the sixth power. It provided the basis for column shape iteration, where the buckling issue is no longer related to uniform cross-section.

The terminology "The shape of the strongest column" was proposed by Keller (1960), which represented the optimum shape of pin-ended column should be convex equilateral triangular cross-section with tapered ends and the moment of inertia was related to cross-sectional area by a quadratic function. By doing so, the buckling load of optimised column increased by 61.2% than that of a circular cylinder, based on both linear and nonlinear buckling states. Two years later, columns with other boundary conditions were investigated by Tadjbakhsh and Keller (1962). According to Keller's research, the optimum shape of pinned column had zero cross-section area at ends, since the bending stress is zero. Trahair and Booker (1970) settled this issue by defining a length ratio of equivalent uniform column and actual column, based on which the lengths of uniform cross-section at ends were determined.

Based on the previous study, Cox and Overton (1992) established and tested an algorithm to determine a column's maximised Euler buckling load under different boundary conditions, which could be widely applied in general design cases. Moreover, they also resolved and corrected the necessary conditions of Tadjbakhsh and Keller by accounting for multiple least eigenvalues.

Instead of stress and displacement in structures, Manickarajah et al. (2000) created an iterative procedure, focusing on the structural stability and dynamic behaviour, based on which the materials in structural members were shifted to the weakest regions with total volume unchanged. Numerical examples of pinned column, portal frame and space frame were implemented and demonstrated the effectiveness of the algorithm.

Apart from the circular solid and hollow section columns, Laghi et al. (2020) designed and manufactured a diagrid column which is optimised by combining the sinusoidal and hyperbolic shape functions with minimised weight. According to the utilisation factor diagram delivered in this article, it was controversial to say that the diagrid column that combined two function shapes benefited from shape optimisation, since the average utilisation factor was lower than that of the reference one, attesting that more materials could be removed to further lower the material consumption.

The optimisation of columns with I-section were investigated by Maria Duque (2022), which aimed to achieve a uniform utilisation factor along the column. Duque modelled the slender I-section columns with varying web cross-sections and conducted the LBA and GMNIA using FE analysis package ABAQUS, which indicated that the optimum geometry for sinusoidal I-section column is 73.5 mm initial height with 90.2 mm height at the middle. The utilisation factor diagram proved that the optimised column could be uniformly utilised along the its length against major axis buckling.

Except optimising by changing column shapes, some design and research works investigated the possibility for perforated web in columns to save materials and gain a higher major axis moment capacity, compared with plain-webs column. Due to the constraint of traditional fabrication method, most of the openings in perforated members investigated up to now were regular geometries, such as rectangular, hexagonal, circular and sinusoidal patterns (Durif & Bouchair, 2016).

Based on various opening patterns, the buckling issue for perforated columns were investigated by Sweedan et al. (2009), where the major axis global buckling was focused and a non-dimensional reduction factor β was proposed for buckling capacity estimation based on the numerical analysis. The major axis global buckling of castellated columns was further investigated by El-Sawy et al. in 2009. In their study, the critical buckling load of castellated columns in a variety of geometries under different boundary conditions were evaluated using the associated equivalent section properties. The design rules of castellated members for major axis buckling was proposed by Sonck and Belis in 2016, which includes the impact of residual stress and imperfections.

In accordance with previous studies, the reduction in major axis buckling capacity of cellular and castellated was mainly induced by the shear and flexural deformations in web, which was commonly observed in perforated beams and named as Vierendeel mechanism (Chung et al., 2001). When the web-post is subjected to the vertical loading, the tensile and compressive forces will transfer through the post and form concentrated compression region adjacent to openings as shown in **Figure 2.3** below. In terms of the axially loaded cellular and castellated columns, the impact of shear deformations on the reduction of buckling capacity becomes less significant when the column length and web post width increase, which also works when the opening height becomes smaller (El-Sawy et al., 2009).

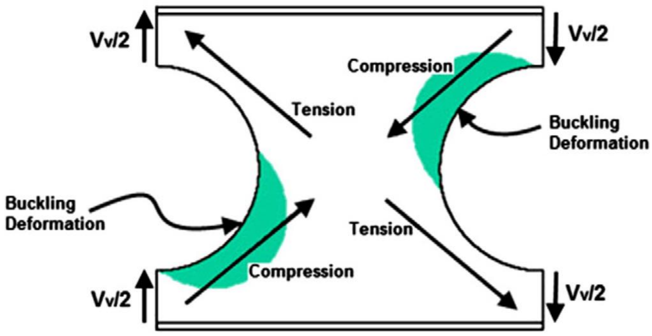

(a) Typical web-post behaviour

(Tsavdaridis & D'Mello, 2011:p.1615)

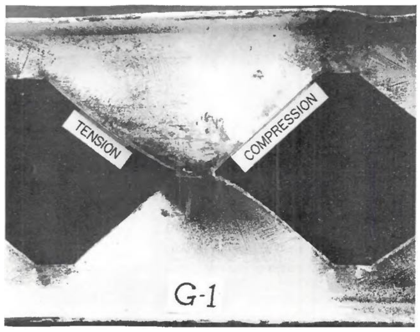

(b) Web buckling failure due to shear

(Hosain & Spiers, 1973:p.338)

Figure 2.3: Web post failure for cellular and castellated columns

Moreover, the minor axis flexural buckling problem of cellular and castellated columns was also investigated in 2016 by Sonck and Belis, based on numerical analysis using ABAQUS. The results of reduction factor χ showed a well agreement with buckling curve c and d proposed in Eurocode 3.

The optimisation cases mentioned above have taken the fabrication issue into account, which were relatively conservative and did not maximise the structural and material efficiency. However, when the additive manufacturing technology was invented, developed and applied in the construction sector, the fabrication issue is no longer the priority that constraints the structural optimisation.

2.2.3 Topology optimisation

In 1870, the initial idea of topology optimisation was proposed by Maxwell, and further developed by Michell in 1904. In the early stage of topology development, the full stress design criteria was widely applied for statically determinate structures, which gave the minimum weight design schemes (Maxwell, 1870; Cilley, 1900; Michell, 1904). In the past decades, many topology optimisation algorithms were developed to leverage the computing power to optimise the structures based on some targets oriented by mass or stiffness.

At present, the frequently applied techniques for topology optimisation are the density-based method (Bendsøe, 1989), the phase-field approach (Bourdin & Chambolle, 2003), the evolutionary approaches (Xie & Steven, 1993), the topological derivative method (Sokolowski & Zochowski, 1999) and the level set method (Allaire et al., 2002; Wang et al., 2003).

Among these mentioned techniques, the density-based method proposed by Bendsøe is one of the leading approaches in topology optimisation, which is also called solid isotropic material with penalisation (SIMP). It aims to find the optimal material distribution by maximise or minimise the objective functions under specific constraints which is normally volume fractions in computational domain. Compared with density-based approach, the phase-field method also works on the density variable with target functions, but there are two phases introduced as void and fictitious liquid which has the pressure force interacted with the solid structure (Bourdin & Chambolle, 2003).

As for the evolutionary approach, the material layouts are determined by the stress solution, based on which the lightly stressed materials in domain will be removed during the iterations. Moreover, the topological derivative method was proposed on the basis of bubble-method, where the impact of creating infinitesimal holes in reference domain was evaluated and gave the solution for the hole's locations in the next iteration. While, the level set method aims to benefit from both the shape sensitivity method and the topology approach, based on which the models are updated by shape derivatives and the level targets will be achieved using topology derivatives (Allaire et al., 2002).

The applications of topology optimisation in structural engineering were reported in recent years, which comprise both cross-section and overall geometry optimisation with different materials. Stromberg et al. (2012) explored the optimal layout of the braced frame for high-rise buildings under discrete loads using combined column elements and quadrilateral elements which offers a new methodology for bracing system design. Moreover, Tsavdaridis et al. (2015) conducted the optimal design for perforated I-section beam based on SIMP, and compared the topology solution with cellular beam as shown in **Figure 2.4**. It is concluded that the stiffness and load capacity were improved for topology optimised beam, based on which concept a cross-bracing web opening was further proposed to ease the manufacturing process.

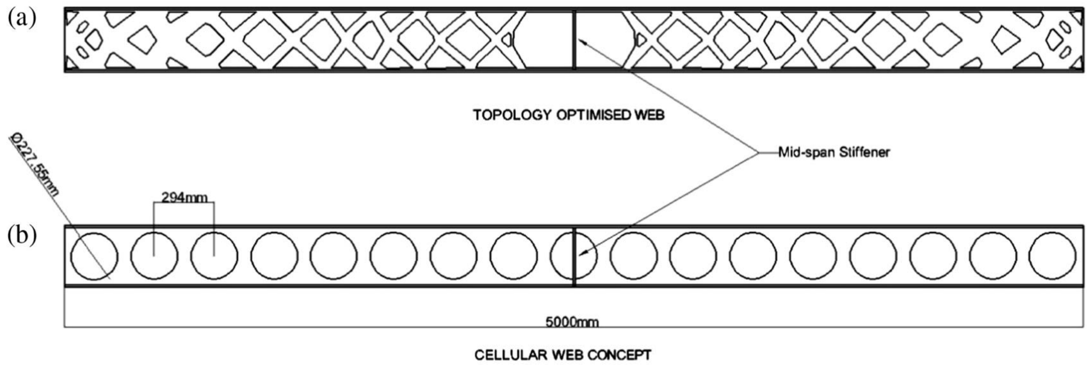

Figure 2.4: (a) Topology optimised and (b) cellular beams (Tsavdaridis et al., 2015:p.113)

In the field of structural engineering, accompanied by metal WAAM, some of the topology optimisation outputs were came to reality from computers. Ye et al. (2021) investigated the optimal geometry and cross-section for tubular trusses and cantilevers. Then, the optimised structures were printed by MX3D based on WAAM as shown in **Figure 2.5(a)**. In cooperation with MX3D, a Japanese architecture company TAKENAKA also carried out a topology optimisation and produced the physical joints by metal WAAM as shown in **Figure 2.5(b)**.

(a) Cantilever truss before and after sandblasting. (Ye et al., 2021:p.165488)

(b) TAKENAKA steel connector (MX3D, 2019)

Figure 2.5: Physical specimens of topology optimisation produced by metal WAAM

These studies concerning topology optimisation and WAAM initially investigated the basic framework for the procedures of topology optimisation based design from concept generation to product fabrication, which lead the direction of future advanced structural design in industry.

2.3 Research significance

As introduced before, the flexural buckling capacity is considered as a target in the column optimisation. However, in accordance with the literature review, the majority of studies only focused on the optimisation of extreme fibres which were done by changing the column shape. The studies related to columns with perforated web were limited, in which attention was mainly paid to buckling capacity and behaviour. Besides, there are no relevant studies concerning the investigation of column optimisation against buckling by creating central opening in web with cross-bracings connecting the flanges, which is inspired by the output of topology optimisation for major axis bending.

Moreover, no research has been conducted to determine how the dimensions of the central opening and cross-bracings affect the response of the web in an axially loaded I-section columns. Considering the change in the dimensions of the effective region of the web sections which will result in new stress distributions in the column cross-sections, further investigation should take place in order to determine how these features influence the column behaviour. Additionally, as an advanced optimisation method, the topology optimisation could be applied in this case to give the optimum material layout in the web section, which has not been mentioned in previous research works.

Therefore, in this dissertation the parametric studies will be performed firstly to investigate the impact of the opening and cross-bracing dimension on column buckling capacity. Then, accompanied by nonlinear topology optimisation, the optimum geometry of the thin-walled I-section column will be further investigated.

Chapter 3 — Finite Element Modelling

3.1 Introduction

In this project, the FE analysis package ABAQUS was employed to conduct the LBA, GMNIA and topology optimisation, which has been widely used in FE modelling and analysis in both academia and industry (Dassault Systemes Simulia Corporation, 2021). As introduced before in Chapter 1, all the columns investigated are 1500.0 mm long, and they could be regarded as medium scale members and will not consume too much computation power, hence the full scale (1:1) FE models were built in ABAQUS. Furthermore the modelling process in this project was aided by Python scripts which will be introduced separately for parametric study and topology optimisation.

3.1.1 Modelling in parametric study

Controlled by python scripts, the parametric study was fully automated, including the creation of the geometries and meshes, setting up boundary conditions, loading and changing parameters. In this parametric study, there were four parameters involved which are the length and height of central opening and the width and spacing of cross-bracings. When the opening was created in web, the web volume, $V_{w,i}$, could be read in ABAQUS using scripts, based on which the total volume of materials removed then was calculated. Then, to maintain the total volume of column unchanged, the amplitude of the sine function for web modelling was recalculated based on the **Equation 3.1** as follows:

$$V_i = H_{in} \cdot L + 2 \cdot \left\{ t_w \cdot \int_0^{\pi} a_{mod} \cdot \sin\left(\frac{\pi \cdot x}{L}\right) dx + b_f \cdot t_f \cdot \int_0^{\pi} \sqrt{1 + \left[a_{mod} \cdot \sin\left(\frac{\pi \cdot x}{L}\right)\right]^2} dx \right\} \quad (3.1)$$

Where,

V_i is the total volume of column, calculated by $V_i = V_{w,ref} + \Delta V_i$.

$V_{w,ref}$ is the volume of web in the reference column from ABAQUS, $V_{w,ref} = 404966.69\ mm^3$.

ΔV_i is the volume of material removed from web, calculated by $V_{w,ref} - V_{w,i} = \Delta V_i$.

H_{in} is the initial height of column (centreline dimension), $H_{in} = 70.0\ mm$.

L is the column length, $L = 1500.0\ mm$.

t_w is the web thickness, $t_w = 3.5\ mm$.

a_{mod} is the modified amplitude of web.

b_f is the flange width, $b_f = 40.0\ mm$.

t_f is the flange thickness, $t_f = 3.5\ mm$.

After obtaining the geometry of columns, the material model, loading, boundary conditions and the meshes were generated, which will be elaborated in detail in the following sub-sections. The framework of the overall modelling and simulation procedures is summarised in **Figure 3.1**.

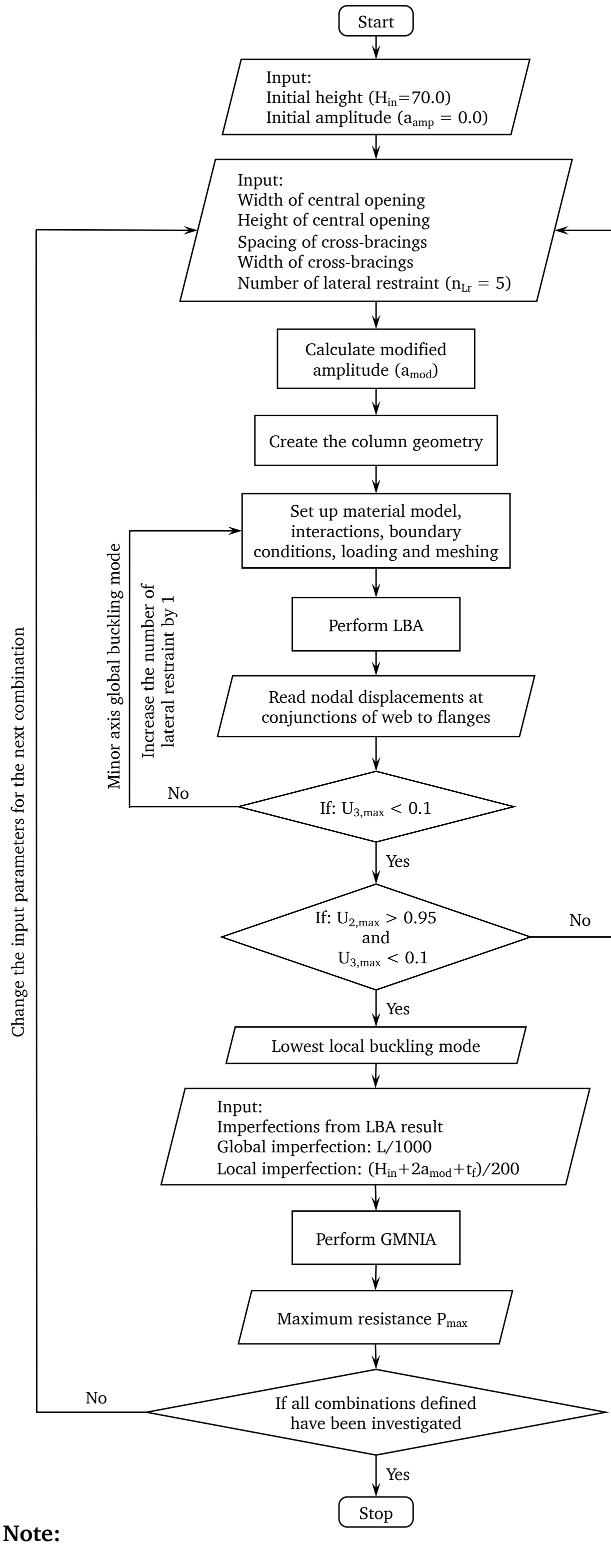

Note:
$U_{3,max}$ is the maximum displacement perpendicular to web (1st eigenmode)
$U_{2,max}$ is the maximum transverse displacement perpendicular to flanges (1st eigenmode)

Figure 3.1: Framework of script used in parametric studies

It is noted that the nodal displacement solution is used to primarily judge the failure mode in each model. Considering that the deformation induced by local buckling modes mainly locates within the web or flanges, the nodes at the conjunctions of web and flanges were employed, where the nodal displacements were not significantly affected by those unexpected local buckling modes. The following illustration in **Figure 3.2** will be of help with clarifying the directions of displacement inspected.

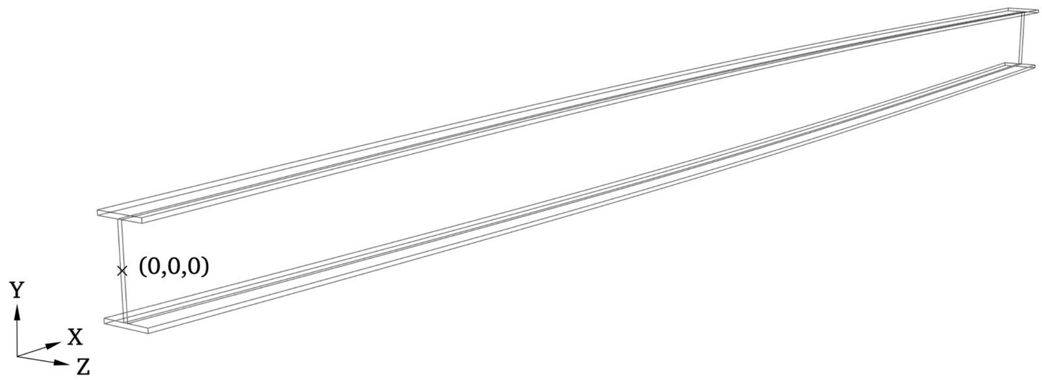

Figure 3.2: Perspective view of the column geometry

Then, the detailed information for the rest of settings in ABAQUS will be introduced separately, from **Section 3.2** to **3.6**.

3.1.2 Modelling in topology optimisation

The topology optimisation were conducted in ABAQUS, employing the programme TOSCA Structure based on the SIMP algorithm. For this density-based optimisation method, the computational domain was defined first, which located within the web section. In this case, a large partition was created in web as shown below in **Figure 3.3**.

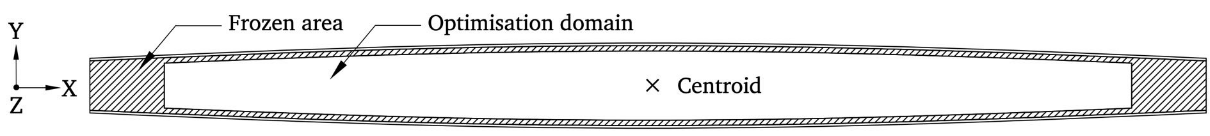

Figure 3.3: General layout of column model in topology optimisation

The central region served as the optimisation domain, in which materials could be removed according to the constrains defined. Then, as shown in **Figure 3.3**, the shaded area in web was defined as a frozen area, where the material density was kept as 1.0 all, to maintain the strength at the ends and conjunction of web and flanges.

This is because the axially loaded thin-walled column web section could be regarded as a thin plate under compression, and the stress distribution in the web cross-section is not uniform (Von Kármán, 1932). It will result in a lightly stressed region near the web neutral axis, which is recognised as the area does not need high material density and stiffness, and will be removed during iterations. However, the materials in frozen area are heavily stressed and the material yielding failure occurs at ends, accompanied by buckling failure in the middle. By constraining the domain within central region, the materials will be kept in frozen web section and flanges to sustain the secondary bending moment and axial load. Furthermore, the dimensions of the frozen area were 100.0 mm at ends and 20.0 mm at the web sections connecting the flanges.

Moreover, the objective function defined in TO was minimising the maximum value of lateral deformation (displacement in the y-direction), by doing which the flexural stiffness will be enhanced during iterations. Furthermore, there were two constraints defined, one was the Von Mises stress constraint and the other was the fraction of volume removed from model. The Von Mises stress was limited below the ultimate strength (636.0 MPa), according to the material model which will be introduced later. While, the volume fraction served as one of the parameters in TO, and it will be described in detail along with **Chapter 5**. Besides, the planar symmetry restrictions were defined about the XZ-plane and YZ-plane with the origin located at the geometric centre of computational domain as indicated in **Figure 3.3**.

Last but not least, similar to parametric study, the total volume of columns were attempted to maintain in the magnitude by increasing the amplitude of web before TO, since the model volume in TO not only depends on the defined volume fraction, but also the mass density which is related to the level of convergence in TO. As TO is a adaptive analysis process, the outcome for each attempts might not be identical. So, compared with the parametric studies, a greater tolerance for volume difference in TO models is accepted.

3.2 Mesh and element type

3.2.1 Mesh pattern

In this research, there were three different optimisation models group, comprising the columns with web constant height ratio opening, opening with tapered ends and TO column models. According to the features of opening, the mesh patterns were different, where various partitions were created to obtain the reasonable mesh layout complying with the geometries. As shown in

Figure 3.4, the typical column models in parametric optimisations with partition for meshing are presented.

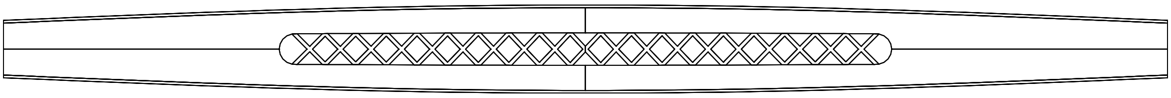

(a) General layout for columns with constant height ratio opening

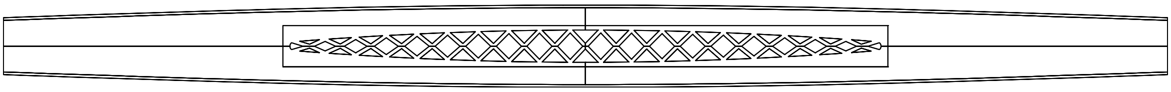

(b) General layout for columns with tapered opening

Figure 3.4: General layout of partitions for column with opening

The meshing technique for cross-bracings within the central partition were Quad-dominated with Advancing front algorithm, which enabled the triangular element to be used at locations with small angles or need mesh transition. Then, for other partitions in both web and flanges, only quadrilateral element was employed and based on Medial axis algorithm. In terms of the models in TO, the quadrilateral elements were used to mesh the whole geometry, similar to the mesh pattern in parametric optimisation model excluding the central region.

3.2.2 Element type and size

In this project, the element type was determined according to the load case and failure mode. Considering that accompanied with the global imperfection, the compression applied at column ends will produce a secondary bending moment, where the bending effects should be taken into account. From the view of shape functions, compared with the linear solid element, the curvature terms in the shell element shape function will give a more accurate prediction of bending stress which makes up the majority of stresses in the critical region at middle. Hence, the shell element comes to top of the list due to its good ability in capture of the bending effects and buckling shape.

Therefore, in ABAQUS the S4R and S3 element was adopted for quadrilateral and triangular elements, respectively. These two elements are both general purpose conventional shell element in ABAQUS shell library, which are based on Reissner-Mindlin formulations normally to account for the shear deformation if a large section thickness is defined (Dassault Systèmes Simulia Corporation, 2014). When section thickness decreases, it becomes discrete Kirchhoff thin shell elements as the shear deformation could be neglected when the shell is thin. The letter R in S4R means reduced integration with hourglass control which helps avoid FE analysis issues including shear locking and spurious mechanism (Dassault Systèmes Simulia Corporation, 2014).

Furthermore, the size of element was selected based on the mesh sensitivity study, in which the size of 1.0 mm, 2.0 mm, 4.0 mm and 8.0 mm were included, and the detailed mesh sensitivity study will be delivered in **Appendix A.1**. Therefore, the element size determined for web sections with openings was 1.0 mm to avoid distorted elements formed in cross-bracings. While for flanges, the mesh size was determined as 4.0 mm to improve computing efficiency, which also ensured the effective connection between web and flanges, and obtained similar level of accuracy. Moreover, the mesh size adopted for TO models was 2.0 mm in both web and flanges.

Hence, the number of nodes in all 375 models for the constant height ratio opening optimisation were range from 59298 to 61386, while for 375 models in tapered opening optimisation, the quantity of nodes were between 112760 to 127690. In terms of the TO models, the number of nodes for all models was 18945, since the column geometry and mesh size were consistent during parametric TO. The typical column model with mesh patterns in topology optimisations are presented in **Figure 3.5**. Whilst, the mesh patterns of model in parametric study will be not presented here, since it is too dense to be well observed.

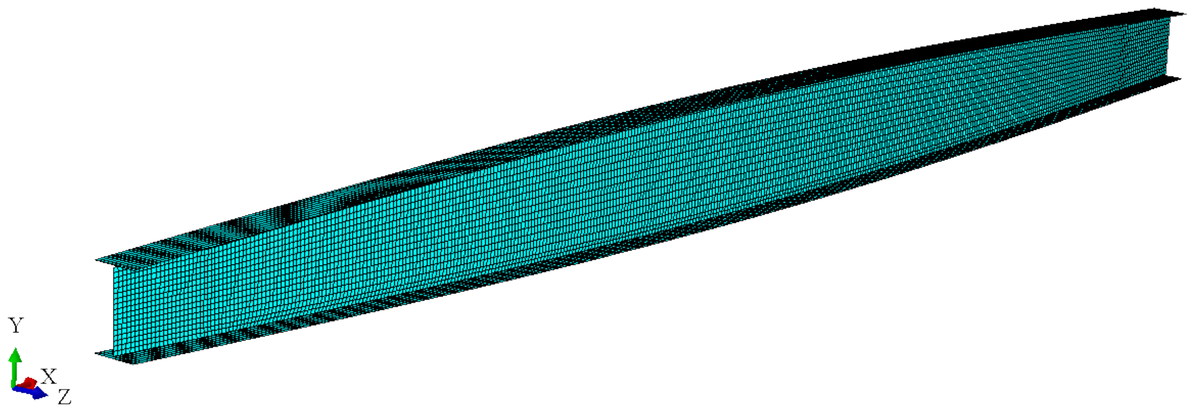

Figure 3.5: Mesh pattern of a typical column model in TO

3.3 Material modelling

The material investigated in this research is S550 carbon steel printed by WAAM. Considering that the test data of WAAM S550 is not available yet, the material model of WAAM is assumed to be the same as hot-rolled carbon steel. Therefore, in this case, the material model of hot-rolled carbon steel proposed by Yun and Gardner (2017) was used to describe the engineering stress-strain curve, as shown from **Equation 3.2** to **3.4**, among which the **Equation 3.2** shows the piecewise function for material stress $f(\varepsilon)$ and the rest two equations present the calculation of ultimate tensile strain and strain hardening strain.

$$\begin{cases} E\varepsilon & \text{for } \varepsilon < \varepsilon_y \\ f_y & \text{for } \varepsilon_y < \varepsilon \le \varepsilon_{sh} \\ f_y + \left(f_u - f_y\right)\left\{0.4\left(\dfrac{\varepsilon - \varepsilon_{sh}}{\varepsilon_u - \varepsilon_{sh}}\right) + 2\left(\dfrac{\varepsilon_u - \varepsilon_{sh}}{\varepsilon_u - \varepsilon_{sh}}\right) \Big/ \left[1 + 400\left(\dfrac{\varepsilon - \varepsilon_{sh}}{\varepsilon_u - \varepsilon_{sh}}\right)^5\right]^{1/5}\right\} & \text{for } \varepsilon_{sh} < \varepsilon < \varepsilon_u \end{cases} \tag{3.2}$$

$$\begin{cases} \varepsilon_u = 0.6\left(1 - \dfrac{f_y}{f_u}\right) \quad \varepsilon_u \ge 0.06 \quad \text{(for hot-rolled steels)} & (3.3) \\ \varepsilon_{sh} = 0.1\dfrac{f_y}{f_u} - 0.055 \quad 0.015 \le \varepsilon_{sh} \le 0.03 & (3.4) \end{cases}$$

According to the coupon tests conducted, the Young's modulus for WAAM S355 and S700 are 201182.0 MPa and 219707.0 MPa, respectively, giving the Young's modulus of 210444.5 MPa for WAAM S550 steel. Then, the yielding and ultimate strength of WAAM S550 steel are 550.0 MPa and 600.0 MPa. Hence, the ultimate tensile strain, ε_u, and strain hardening strain, ε_{sh}, are 0.06 and 0.03, respectively based on **Equation 3.3** and **3.4**.

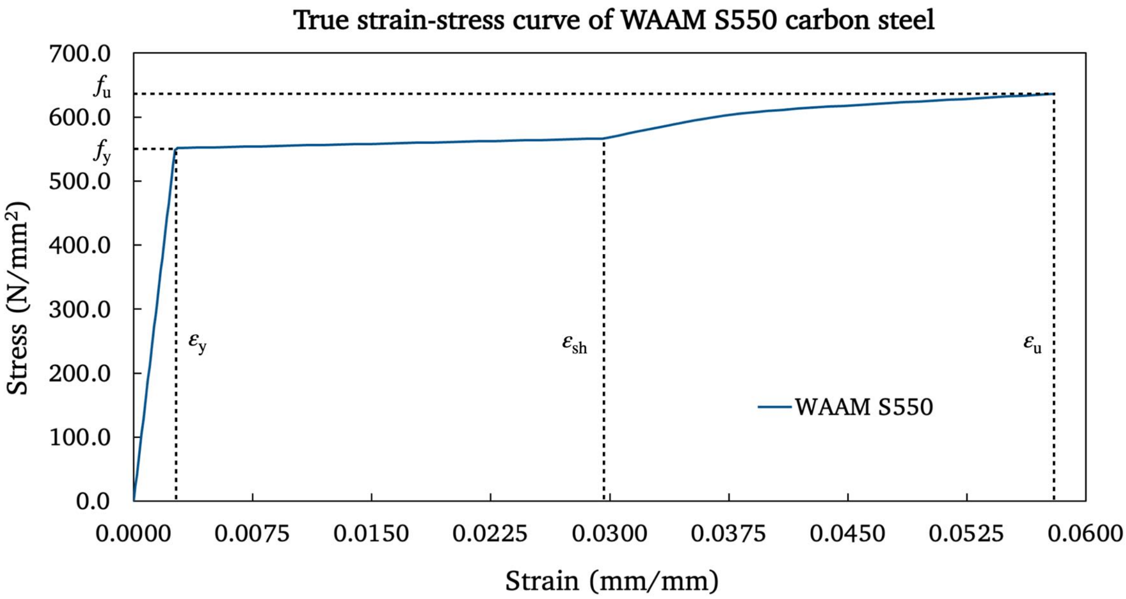

Figure 3.6: True strain and stress curve of WAAM S550 carbon steel

When the steel section is stressed in tension, the poisson effects will induce the shrinkage of cross-section along with section elongation. Therefore, the true strain and stress were calculated from engineering strain and stress based on the correlation proposed by Faridmehr, et al. in 2014. The **Equation 3.5** and **3.6** introduce the true strain and stress in steel under tension.

$$\begin{cases} \sigma_{\text{true}} = \sigma_{\text{eng}} \left(1 + \varepsilon_{\text{eng}}\right) & (3.5) \\ \varepsilon_{\text{true}} = \ln\left(1 + \varepsilon_{\text{eng}}\right) & (3.6) \end{cases}$$

In accordance with the properties introduced, the true stress and strain curve of WAAM S550 was plotted as shown in **Figure 3.6** above. For FE modelling in ABAQUS, the true stress and true plastic strain were defined as the plasticity in material property.

3.4 Interaction

3.4.1 Tie constraint

The flanges and web sections were modelled separately initially and assembled afterwards, thus the tie constraint was employed to connect those separate parts. In this case, the web section have greater stiffness compared with flanges under compression, which was introduced as the master surface as sketched by red curves in **Figure 3.7**, below. The inner flange surfaces were defined as the slave surface in this tie constraint, given the same degree of freedom as web edges. It is noted that, to avoid the volume intersection, there was a gap made between each flange and web, with the distance of a half flange thickness $0.5 \cdot t_{\text{f}}$. Hence, a tolerance of full flange thickness was defined to ensure that the tie constraint will work well with the existing gaps between mid-surfaces.

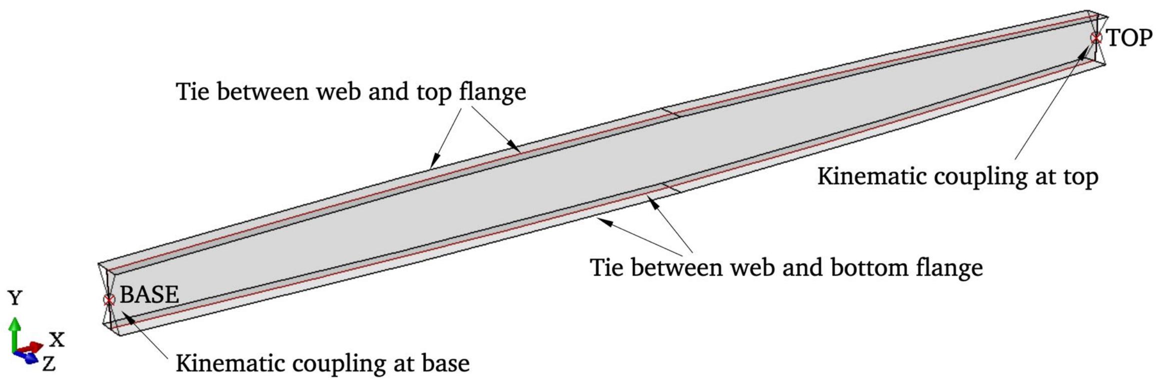

Figure 3.7: General layout of constraints

3.4.2 Kinematic coupling at end sections

The column ends were assumed to be the rigid end conditions, thus no local deformation was allowed with the rotation at end sections. Hence, to realise the rigid condition, two reference points were created at the centre of base surface at (0,0,0) and top surface at (1500,0,0), based on which all the degree of freedoms at base and top end sections were coupled at these two points through kinematic coupling constraints as shown in **Figure 3.7**, above. Then, the mechanical boundary conditions were applied to the reference points, following the assumptions made.

3.5 Boundary and Loading condition

3.5.1 Mechanical boundary condition (BC)

The pin-ended boundary condition was assumed in this research, which was applied to the reference points at base and top of the column as introduced before. In terms of the reference point at base, the all translational degree of freedoms (U_1,U_2 & U_3=0) and rotational degree of freedom (UR_1=0) about longitudinal axis were defined as 0. While, as for BC at top reference point, the only difference was that the translational degree of freedom along longitudinal axis (U_1) was allowed, compared with the base condition.

In addition, to obtain the major axis global buckling failure mode, the lateral restraints were involved to maintain the stability of web. In FE models, the lateral restraints were applied at the points along the conjunction of web and flanges with the only restriction to displacements in the Z-direction (U_3=0).

3.5.2 Axial load

The displacement controlled axial loading was defined at reference point at top of column towards the negative direction of the X-axis with the magnitude as -10.0 mm. In this case, the end shortening at failure were around 5.0 mm, based on which the column behaviours before and after collapse could be well captured. Besides, the value of load applied along loading would be obtained by the reaction force in the X-direction (RF_1). Combined with end shortening and lateral deformation at mid-span, the load-deformation diagrams could be plotted.

3.5.3 Equivalent lateral load (only for topology optimisation)

The additional lateral load was applied for topology optimisation models specifically, aiming to tigger the global bow imperfection in TOSCA Structure. The value of equivalent lateral load was calculated based on the formulations provided in Eurocode 3, Section 5.3.2(7), as shown in **Equation 3.7** (British Standards Institution, 2005).

$$w = \frac{8N_{Ed}e_{0,d}}{L^2} = \frac{8 \times 286.9 \times 1.5}{1500.0^2} = 1.54 \text{ kN} \tag{3.7}$$

Where,

N_{Ed} is the design load, taken as collapse load (P_{max}).

L is the column length, L = 1500.0 mm.

$e_{0,d}$ is the global imperfection, $e_{0,d} = L/1000 = 1.5$ mm.

Hence, a 1.54 kN shell edge load was applied along one of the web edge to replace the initial bow imperfection. The following **Figure 3.8** shows the summarised overall boundary and loading conditions for TO, where all the BCs defined in parametric studies are also included.

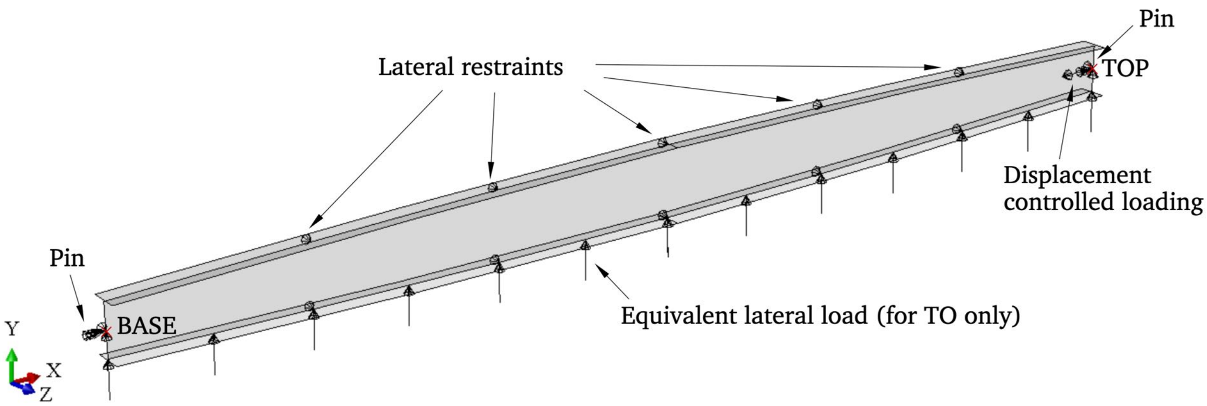

Figure 3.8: General layout of boundary and loading conditions

3.6 Geometric imperfection

In this research, considering the web with opening and cross-bracings might easily suffer from the local buckling, both the global buckling and local buckling imperfections were applied as mesh perturbation in GMNIA. The modelling of imperfections was based on the results of LBA and the elastic buckling mode shape in the first eigenmode was taken as the global imperfection, then the shape in lowest local buckling mode was assigned as the local imperfection in GMNIA as shown in **Figure 3.9**.

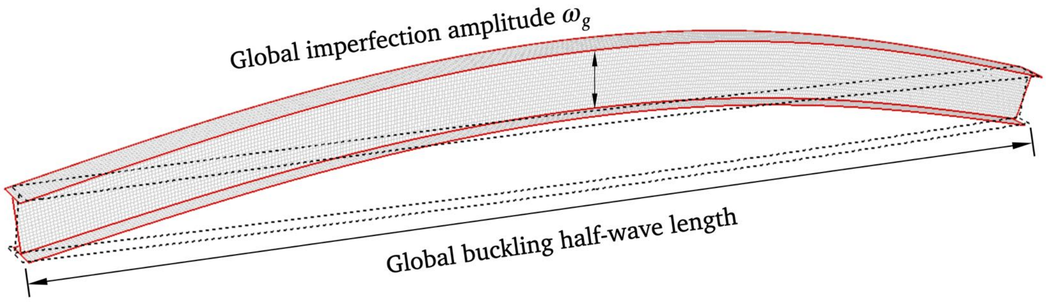

(a) Typical global imperfection mode

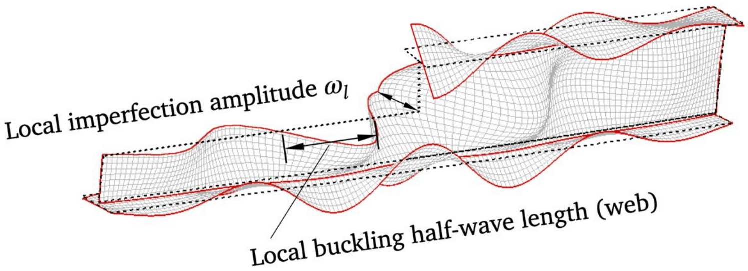

(b) Typical local imperfection mode (cut section shown for clarity)

Figure 3.9: Definitions of imperfection amplitude and half-wavelength for GMNIA

The amplitude of global imperfection was set as ω_g= L/1000, used in the column buckling curves in the Eurocode 3, which also been proved to provide the accurate buckling load by FE analysis compared with experiments (Tuezney et al., 2021). While, as for local imperfection, a reasonable value of ω_l= d/200 was used as the amplitude, where the “d” indicates the largest width of column, between outer surfaces of flange (El-Adly et al., 2011). As the geometry of column changed with different opening patterns, the amplitude was automatically calculated by scripts, and defined in GMNIA.

Chapter 4 — Validation of the FE Model

4.1 Model verification

Due to lack of experiment data, the FE model will be verified in accordance with the analytical elastic buckling load under major axis global buckling herein. The FE model of reference column with uniform cross-section was developed following the steps described above. The young's modulus used in validation is 210444.5 MPa as introduced. The second moment of area for major axis buckling is obtained as:

$$I = \sum \frac{bh^3}{12} + \sum Ad^2 = \frac{5 \times 30^3 + 2 \times 40 \times 5^3}{12} + 2 \times 40 \times 5 \times 17.5^2 = 134583.33\ \text{mm}^4$$

Then, the critical buckling load predicted by the Euler column formula is calculated as follows:

$$P_{cr} = \frac{\pi^2 EI}{L_{cr}^{\ 2}} = \frac{\pi^2 \times 210444.5 \times 134583.33}{1500.0^2} \times 10^{-3} = 124.24\ \text{kN}$$

Furthermore, the LBA of reference column was performed, in which the axial load defined in FE model was 1000.0 N. Hence, the eigenvalue presented in ABAQUS was directly the critical load in unit of kN. As shown in **Figure 4.1**, the major axis buckling critical load predicted by FE model developed is 127.00 kN.

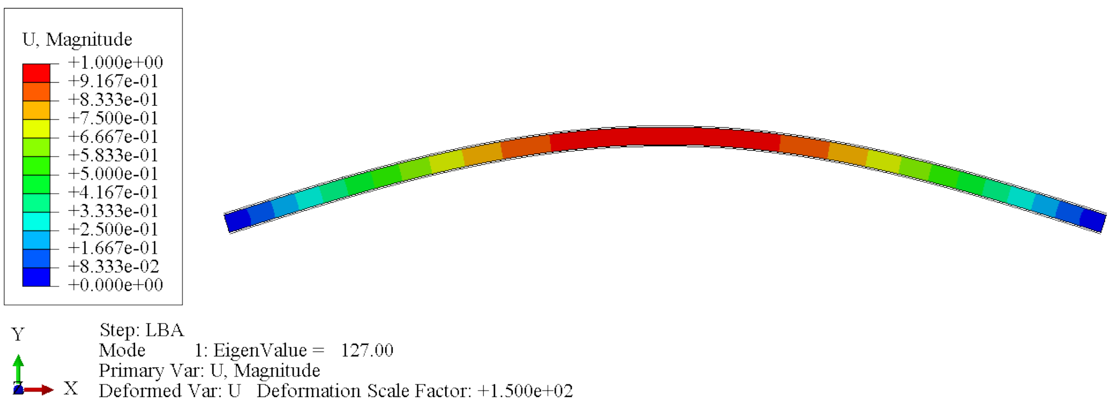

Figure 4.1: FE analysis result of critical buckling load from ABAQUS

The difference between analytical and numerical solution to critical buckling load is only 2.17%. The good agreement between analytical method and numerical simulation mentioned above attests that the structural responses could be well captured by the FE models developed in this research.

Chapter 5 — Results and Discussion

In this study, three attempts of optimisation were conducted, including two attempts of parametric studies and one attempt of topology optimisation. In parametric studies, 750 combinations of opening dimensions (length and height) and cross-bracing spacing and width were considered. Moreover, the LBA was conducted for each combination, whereas the GMNIA was only performed for columns with major axis global buckling as the lowest eigenmode. In terms of topology optimisation, the FE models with various volume fractions and material interpolation penalty factors were analysed in ABAQUS. In this chapter, the key results of optimised columns, including load and displacement diagrams and Von Mises stress distribution graphs from GMNIA, will be presented with discussions.

5.1 Parametric study — Web opening (constant height ratio)

5.1.1 Model introduction

Upon the FE model validation, the numerical parametric studies were carried out focusing on the column optimisation with constant height ratio (CHR) web opening. As previously mentioned, four parameters were studied, including the opening length and height, as well as the spacing and width of the cross-sections. With the assistance of a Python script, the geometry of columns with constant height ratio openings was generated directly in ABAQUS. As shown in **Figure 5.1**, the shape function of web opening is derived by multiplying the Y-coordinates of the vertices of the web edge by a constant ratio. At the ends of the central opening, two half circles were implemented to moderate the stress concentration.

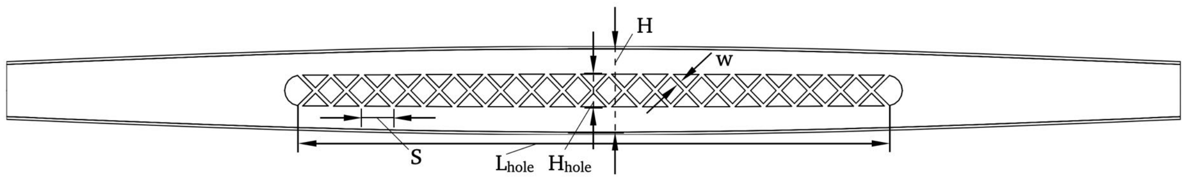

Figure 5.1: General layout of column model with CHR opening

Furthermore, the four dimension parameters involved in this parametric study were illustrated in **Figure 5.1**, and the values investigated were listed in **Table 5.1**, as follows.

Table 5.1: Parameters investigated in parametric studies (unit: mm)

Index	Length of opening (H_{hole})	Height of opening (L_{hole})	Spacing of cross-bracing (S)	Width of cross-bracing (w)
1	450.0 (R_L = 0.3)	26.01 (R_H = 0.3)	20.0	3.5
2	600.0 (R_L = 0.4)	34.68 (R_H = 0.4)	30.0	5.0
3	750.0 (R_L = 0.5)	43.35 (R_H = 0.5)	40.0	7.0
4	900.0 (R_L = 0.6)	52.02 (R_H = 0.6)	50.0	—
5	1050.0 (R_L = 0.7)	60.70 (R_H = 0.7)	60.0	—

It is noted that the R_L (L_{hole}/L) represents the ratio of opening length to the total column length 1500.0 mm, whilst the R_H (H_{hole}/H_{ref}) indicates the ratio of opening height to the web width of the reference column which is the web dimension with before modifying amplitudes to get the constant volume. Additionally, the column models were labelled by "R_L+R_H+S+w" in this study.

5.1.2 Results of collapse load from GMNIA

In this optimisation, 375 combinations were considered, among which the models will be primarily grouped according to the width of the truss, which is relatively discrete in comparison with the other three parameters. Among all these combinations, 268 models passed the major axis buckling check, from which the results of collapse load were recorded. However, in this section, only the significant results are presented, where the opening height served as the second parameter for sub-classification. Then, the maximum collapse load for models with the same cross-bracing width and opening height will be found within all combinations of opening length and spacing of cross-bracings. In the following **Figure 5.2**, the load-deformation curves from models with each opening height and bracing width are plotted against the reference column, whose maximum resistance was obtained as 286.90 kN.

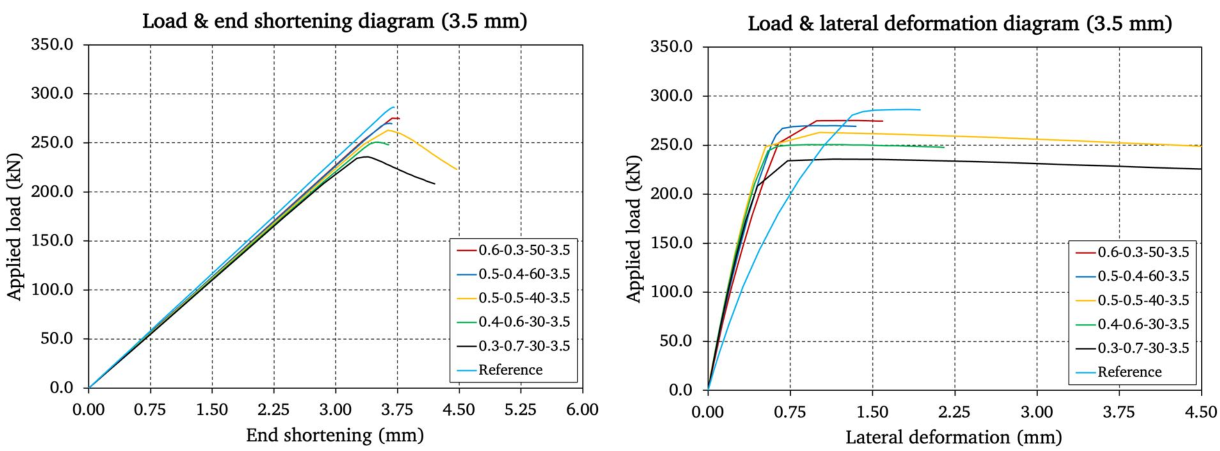

(a) Load-end shortening curves (3.5 mm) (b) Load-lateral deformation curves (3.5 mm)

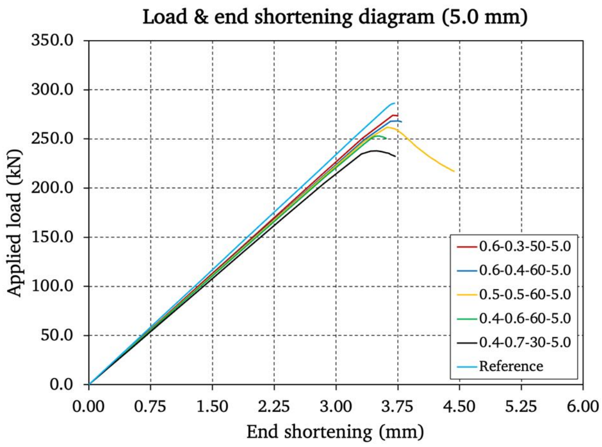

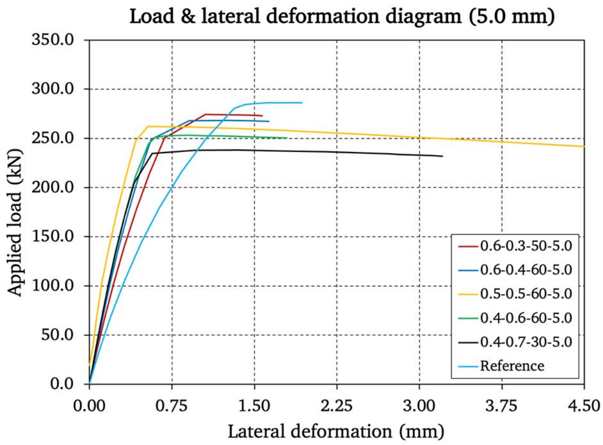

(c) Load-end shortening curves (5.0 mm) (d) Load-lateral deformation curves (5.0 mm)

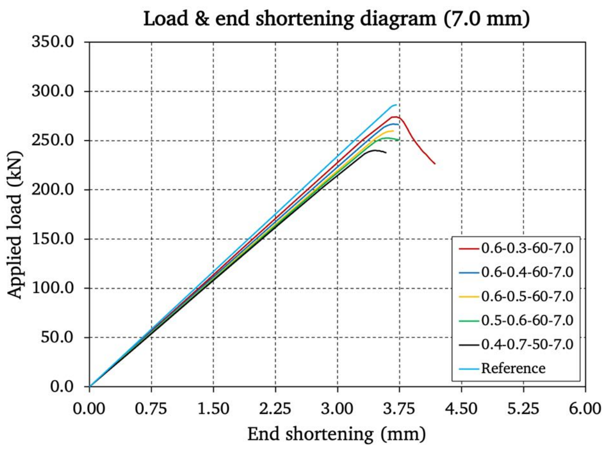

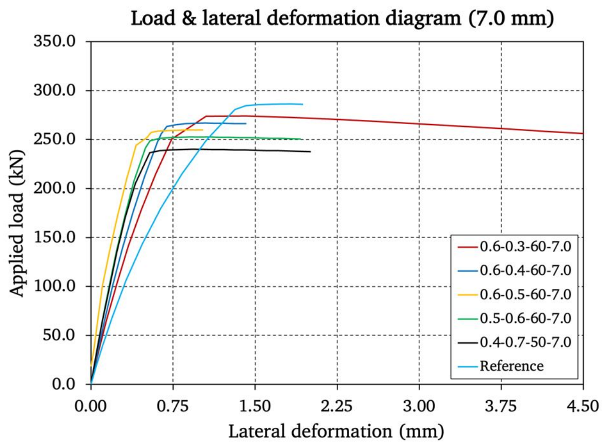

(e) Load-end shortening curves (7.0 mm) (f) Load-lateral deformation curves (7.0 mm)

Figure 5.2: Load-deformation curves for column with CHR opening (varying bracing widths)

According to the load-deformation curves presented above, all collapse loads from column models with openings are less than the maximum resistance of the reference column with the same total volume. A similar failure mode could also be observed for all models presented, which is global buckling interacting with local buckling. It is clearly shown in **Figure 5.2 (b), (d)** and **(f),** that the lateral stiffness of columns with opening was enhanced compared with that of benchmark column, as the gradients became greater. Then, the results of maximum resistance (P_{max}) in this parametric study are summarised in **Table 5.2** below.

Table 5.2: Summary of maximum resistance for columns with CHR opening

Index	w (mm)	L_{hole} (mm)	H_{hole} (mm)	S (mm)	P_{max} (kN)	δ_{ref}
1	3.5	900.0 (R_L = 0.6)	26.01 (R_H = 0.3)	50.0	275.15	-4.1%
2	3.5	750.0 (R_L = 0.5)	34.68 (R_H = 0.4)	60.0	269.84	-5.9%
3	3.5	750.0 (R_L = 0.5)	43.35 (R_H = 0.5)	40.0	262.90	-8.4%
4	3.5	600.0 (R_L = 0.4)	52.02 (R_H = 0.6)	30.0	250.61	-12.6%
5	3.5	450.0 (R_L = 0.3)	60.70 (R_H = 0.7)	30.0	235.68	-17.9%
6	5.0	900.0 (R_L = 0.6)	26.01 (R_H = 0.3)	50.0	274.16	-4.4%
7	5.0	900.0 (R_L = 0.6)	34.68 (R_H = 0.4)	60.0	268.29	-6.5%
8	5.0	750.0 (R_L = 0.5)	43.35 (R_H = 0.5)	60.0	262.01	-8.7%
9	5.0	600.0 (R_L = 0.4)	52.02 (R_H = 0.6)	60.0	253.08	-11.8%
10	5.0	600.0 (R_L = 0.4)	60.70 (R_H = 0.7)	30.0	237.97	-17.1%
11	7.0	900.0 (R_L = 0.6)	26.01 (R_H = 0.3)	60.0	274.01	-4.5%
12	7.0	900.0 (R_L = 0.6)	34.68 (R_H = 0.4)	60.0	266.75	-7.0%
13	7.0	900.0 (R_L = 0.6)	43.35 (R_H = 0.5)	60.0	259.73	-9.5%
14	7.0	750.0 (R_L = 0.5)	52.02 (R_H = 0.6)	60.0	252.56	-12.0%
15	7.0	600.0 (R_L = 0.4)	60.70 (R_H = 0.7)	50.0	239.98	-16.4%

Note: δ_{ref} represents the difference in P_{max} between column with opening and the reference column.

As indicated in both load-deformation curves and tabulated results, the height of the opening turns out to be one of the significant factors that affect the level of collapse load. As the opening height becomes greater, the collapse load drops significantly, regardless of the opening length, bracing spacing and bracing width. Moreover, according to the magnitude of δ_{ref}, it is apparent that the decrease of bracing width slightly helps mitigate the loss of resistance, when the opening height ratio is below 0.7.

However, for the columns with CHR opening investigated, the maximum resistance achieved in models with CHR opening is 275.15 kN based on which the optimisation target was not achieved, as all the models involved in the combination had less maximum resistance than the benchmark value. Therefore, the effects of introducing CHR openings on column failure modes should be further analysed based on the stress distribution and deformation contour graphs.

As presented below in **Figure 5.3**, the von Mises stress distribution at the increment of failure for the strongest column with CHR opening within this study is shown, where the grey regions indicate the yielded fibres. The scale factor was set as 50.0 to give a better view of the geometry deformation at collapse.

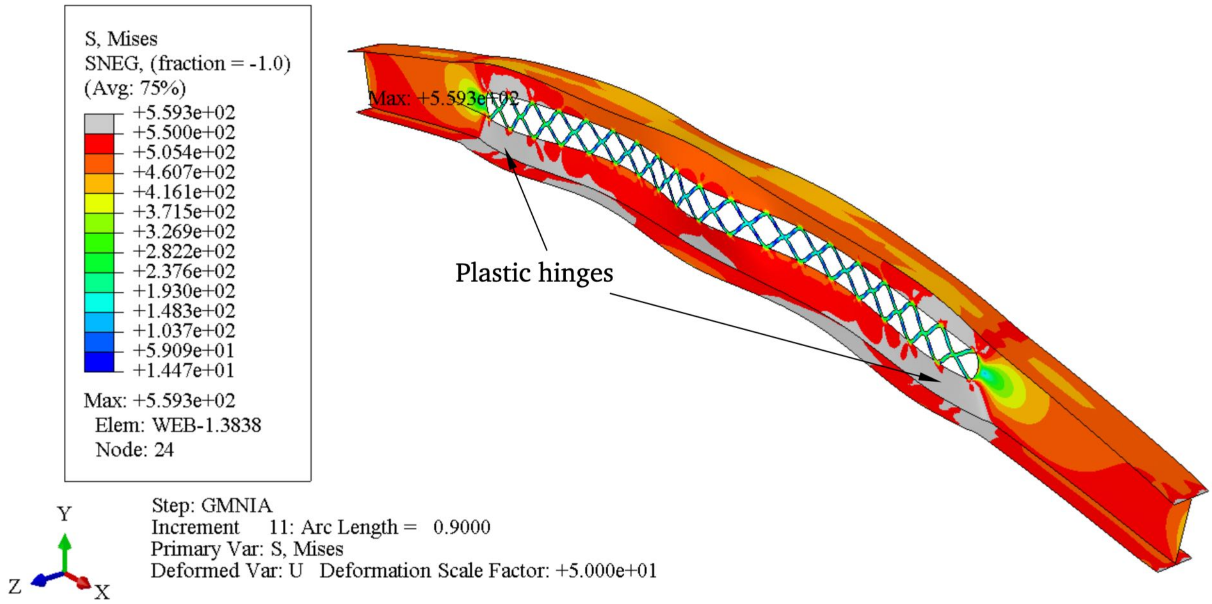

Figure 5.3: Von Mises stress plot at column collapse (model: 0.6-0.3-50-3.5)

Figure 5.3 shows that the level of von Mises stress is relatively high in most areas of both tension and compression zones, indicating a coupled major axis global buckling failure and material yielding mode. Due to the strong middle cross-section in this varying cross-section geometry, the stress level at column ends is approximately at the yielding strength, which indicates that the materials were utilised more efficiently at ends as opposed to a straight column that would fail as a result of pure global buckling.

The plastic hinges were formed in the T-sections near the ends of the opening when the column collapsed. In order to show the formation of these plastic hinges, the von Mises stress distributions in five increments before failure were plotted in the **Figure 5.4(a)** to **5.4(e)**. It is noted that the colour varying from blue to red indicates the increment in stress magnitude between the minimum and maximum stress annotated.

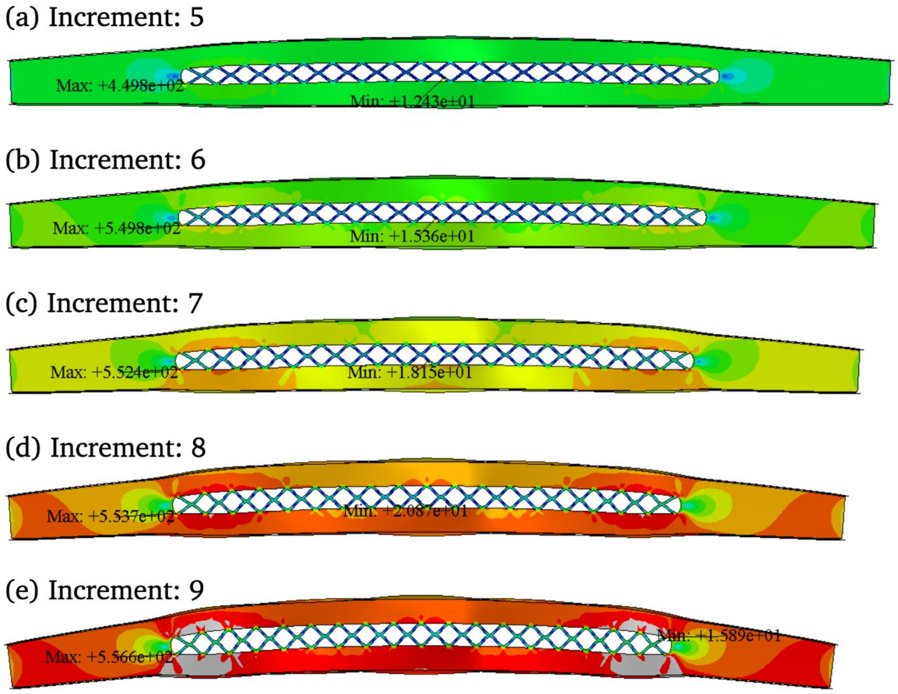

Figure 5.4: History of von Mises stress plot of model: 0.6-0.3-50-3.5 (unit: N/mm^2)

Due to the geometry discontinuity, the compression stress field was split in two by the openings, resulting in two concentrated compression regions, as shown in **Figures 5.4(c)** and **5.4(d)**. Moreover, the local buckling imperfection was introduced in this case, and its maximum amplitude located near these stress concentration zones, due to which the local buckling occurs firstly under excessive compression and followed by the global buckling afterwards.

The following **Figure** 5.5 below gives a clearer view of the stress concentration zone at one end, in which could be observed at the location that the first cross-bracing was connected to the web sections, as the maximum von Mises stress value was labelled. Combined with the local imperfection, the local buckling in T-sections occurred and then developed plastic hinges at the opening ends across the column section, due to which the column gained more flexibility at these hinges and triggered the global buckling failure.

Therefore, in this case, the stress concentration accompanied by the local buckling effects, deteriorated the column bearing capacity and led to a loss of collapse load compared with the reference column. To mitigate this issue, a new version of the opening pattern with tapered ends was introduced, according to the researches concerning the stress concentration in plates and shells with elliptical holes (Pierce & Chou, 1973; Patel & Desai, 2020).

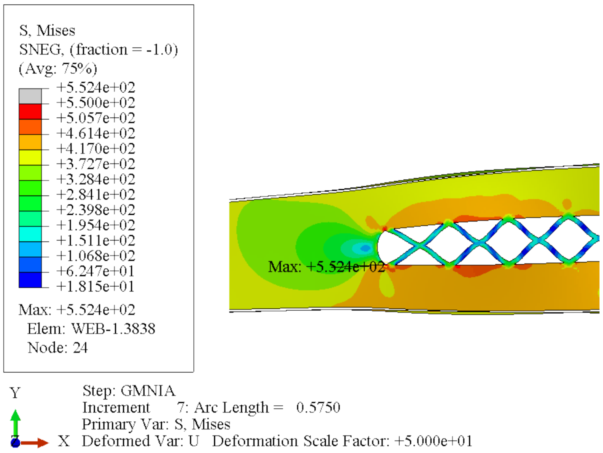

(a) Stress concentration during loading

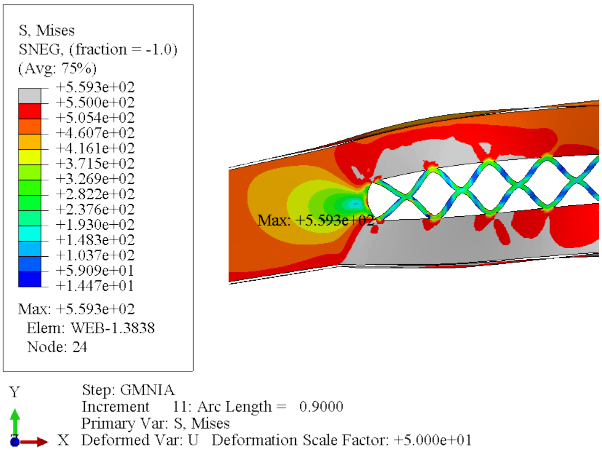

(b) Plastic hinge at collapse

Figure 5.5: Stress concentration and plastic hinge pattern (cut sections shown for clarity)

Due to the tapered ends of the opening, the level of geometry discontinuity is reduced compared to that of a constant height ratio opening, which allows stress to flow more smoothly into the T-sections surrounding the opening. Furthermore, as the opening becomes narrower than before, the ratio of bracing width and opening height near the ends then reduces, which means the cross-bracing will be relatively stronger than before to stabilise the T-sections. Consequently, the local buckling imperfection tends to shift toward the middle, which has the benefit of preventing local buckling from being easily triggered since stress concentration zones and geometric imperfection no longer overlap.

5.2 Parametric study — Web opening (tapered ends)

5.2.1 Model introduction

As introduced in previous section, the shape of opening was updated to further moderate the stress concentration adjacent to the opening at quarters. The gradient of web opening was made shallower than the constant height ratio opening by super-positioning a quadratic function $f(x) = \mathrm{A} \cdot (x - \mathrm{L}/2)^2$ to the web sine function, where the amplitude A is related to the end height of CHR opening with a ratio $\mathrm{R_{end}}$, by controlling which the height at opening ends could be reduced proportionally. In this study, the height of web opening at ends were reduced by 70% ($\mathrm{R_{end}}$=0.3), compared with that of original CHR web openings, whereas the height in the middle remain unchanged. The general layout of columns with tapered opening is illustrated in **Figure 5.6** as follows. Moreover, to keep consistency and better compare the collapse loads, the same parameters were investigated in this parametric study as those engaged in optimisations with

CHR opening. The detailed dimensions of opening and cross-bracings were referred to **Table 5.1**, based on which the same 375 combinations were investigated as well.

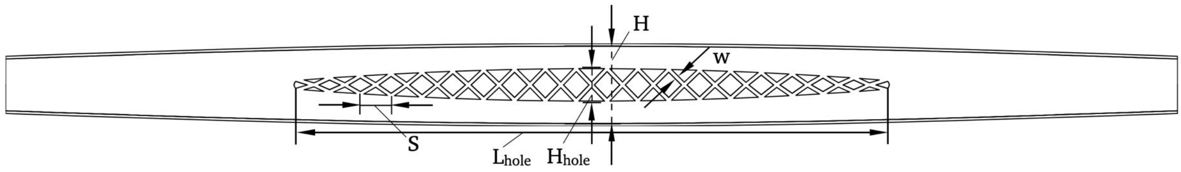

Figure 5.6: General layout of column model with tapered opening

5.2.2 Results of collapse load from GMNIA

For the optimisation with tapered openings, the numerical models were grouped in a similar manner as mentioned in CHR opening optimisation (Section 5.1.2), among which, 225 models obtained the major axis global buckling mode as the lowest eigenmode. Based on these models, the results of collapse load and loading history were recorded and plotted in **Figure 5.7** against the results from reference column.

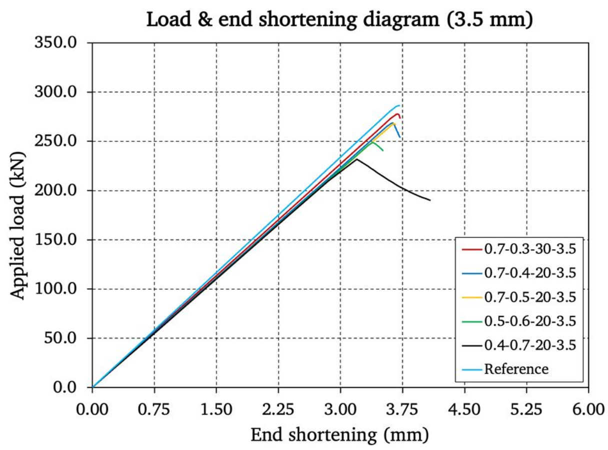

(a) Load-end shortening curves (3.5 mm)

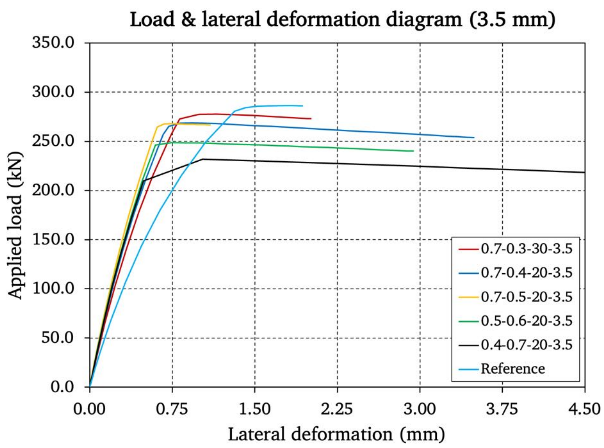

(b) Load-lateral deformation curves (3.5 mm)

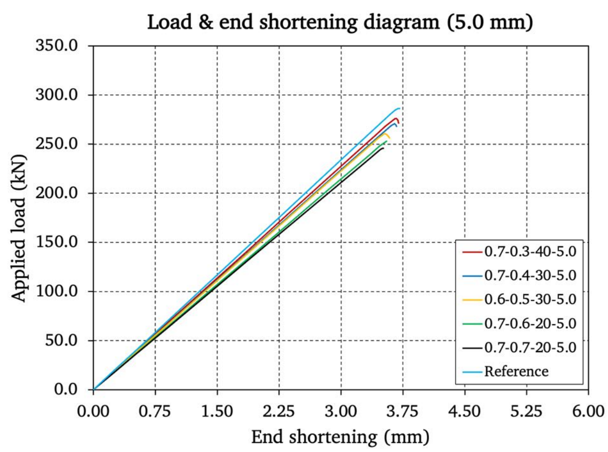

(c) Load-end shortening curves (5.0 mm)

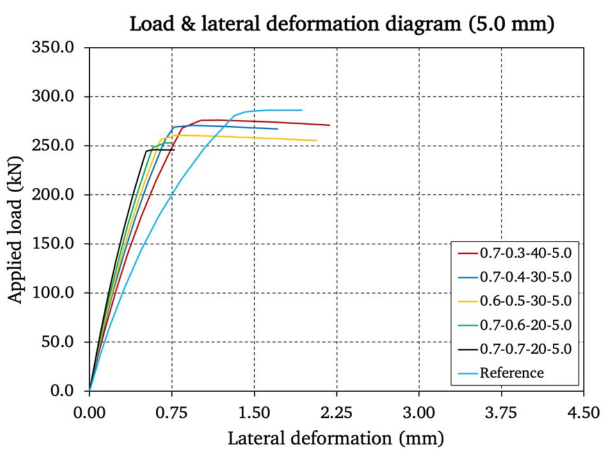

(d) Load-lateral deformation curves (5.0 mm)

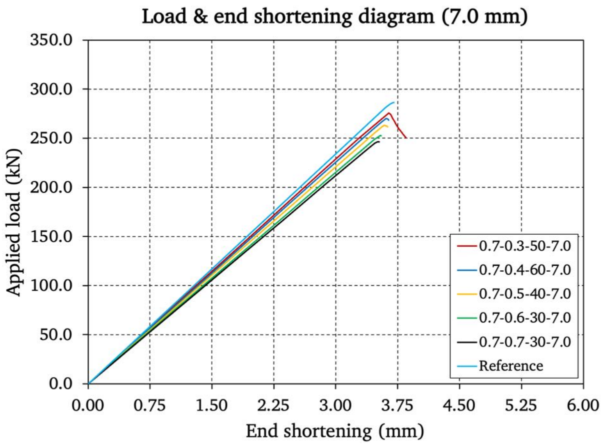

(e) Load-end shortening curves (7.0 mm)

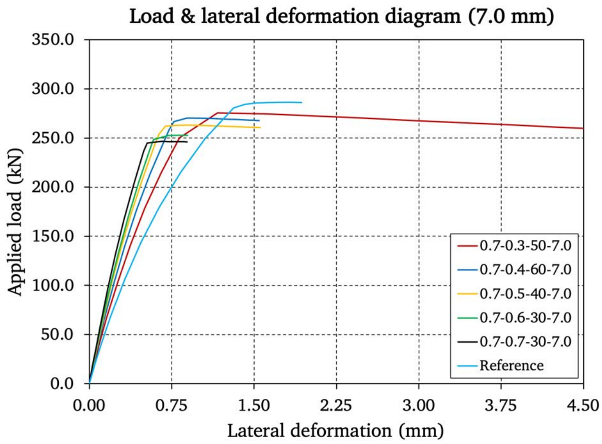

(f) Load-lateral deformation curves (7.0 mm)

Figure 5.7: Load-deformation curves for column with tapered opening (varying bracing widths)

As shown in **Figure 5.7**, the failure mode of columns with tapered openings is similar to that of the reference column, which is dominated by the global buckling failure. Besides, it can be seen in **Figure 5.7(d)** and **5.7(f)** that in the pre-buckling region, the gradients of the load-lateral deformation curve decrease with the reduction of opening height, which means the columns gain more flexural stiffness when the opening height becomes greater. It can be explained by the modification of web geometry to maintain the total volume. For larger openings, the materials removed were placed at the web edges, by which a wider column with a greater second moment of area was obtained. Hence, the larger web opening will lead to a stiffer flexural response. In terms of the axial stiffness of columns with opening, as shown in **Figures 5.7(a)** and **5.7(e)**, the slopes of the load-end shortening curve show a decreasing trend with less axial stiffness obtained from reduced cross-section area, as shown in **Figure 5.7(e)** in particular. The tabulated results of the key models in each combination of bracing width and opening length are delivered in **Table 5.3** as follows.

Table 5.3: Summary of maximum resistance for columns with tapered opening

Index	w (mm)	L_{hole} (mm)	H_{hole} (mm)	S (mm)	P_{max} (kN)	δ_{ref}
1	3.5	1050.0 ($R_L = 0.7$)	26.01 ($R_H = 0.3$)	30.0	277.68	-3.2%
2	3.5	1050.0 ($R_L = 0.7$)	34.68 ($R_H = 0.4$)	20.0	268.83	-6.3%
3	3.5	1050.0 ($R_L = 0.7$)	43.35 ($R_H = 0.5$)	20.0	267.92	-6.6%
4	3.5	750.0 ($R_L = 0.5$)	52.02 ($R_H = 0.6$)	20.0	248.74	-13.3%
5	3.5	600.0 ($R_L = 0.4$)	60.70 ($R_H = 0.7$)	20.0	231.66	-19.3%

Index	w (mm)	L_{hole} (mm)	H_{hole} (mm)	S (mm)	P_{max} (kN)	δ_{ref}
6	5.0	1050.0 ($R_L = 0.7$)	26.01 ($R_H = 0.3$)	40.0	276.08	-3.8%
7	5.0	1050.0 ($R_L = 0.7$)	34.68 ($R_H = 0.4$)	30.0	270.57	-5.7%
8	5.0	900.0 ($R_L = 0.6$)	43.35 ($R_H = 0.5$)	30.0	260.76	-9.1%
9	5.0	1050.0 ($R_L = 0.7$)	52.02 ($R_H = 0.6$)	20.0	252.93	-11.8%
10	5.0	1050.0 ($R_L = 0.7$)	60.70 ($R_H = 0.7$)	20.0	245.92	-14.3%
11	7.0	1050.0 ($R_L = 0.7$)	26.01 ($R_H = 0.3$)	50.0	275.61	-3.9%
12	7.0	1050.0 ($R_L = 0.7$)	34.68 ($R_H = 0.4$)	60.0	270.14	-5.8%
13	7.0	1050.0 ($R_L = 0.7$)	43.35 ($R_H = 0.5$)	40.0	263.03	-8.3%
14	7.0	1050.0 ($R_L = 0.7$)	52.02 ($R_H = 0.6$)	30.0	252.75	-11.9%
15	7.0	1050.0 ($R_L = 0.7$)	60.70 ($R_H = 0.7$)	30.0	246.45	-14.1%

Note: δ_{ref} represents the difference in P_{max} between column with opening and the reference column

For the strongest column with the tapered opening, a 2.53 kN improvement in resistance could be observed compared with the constant height ratio opening pattern in the last optimisation. However, this slight improvement still can not accomplish the goal of column optimisation against buckling, where the maximum column capacity in this study drops by 3.2%, compared with reference P_{max}. The reduction of the collapse load is attributed to the similar failure mode for columns with CHR opening which is local buckling accompanied by the global buckling failure.

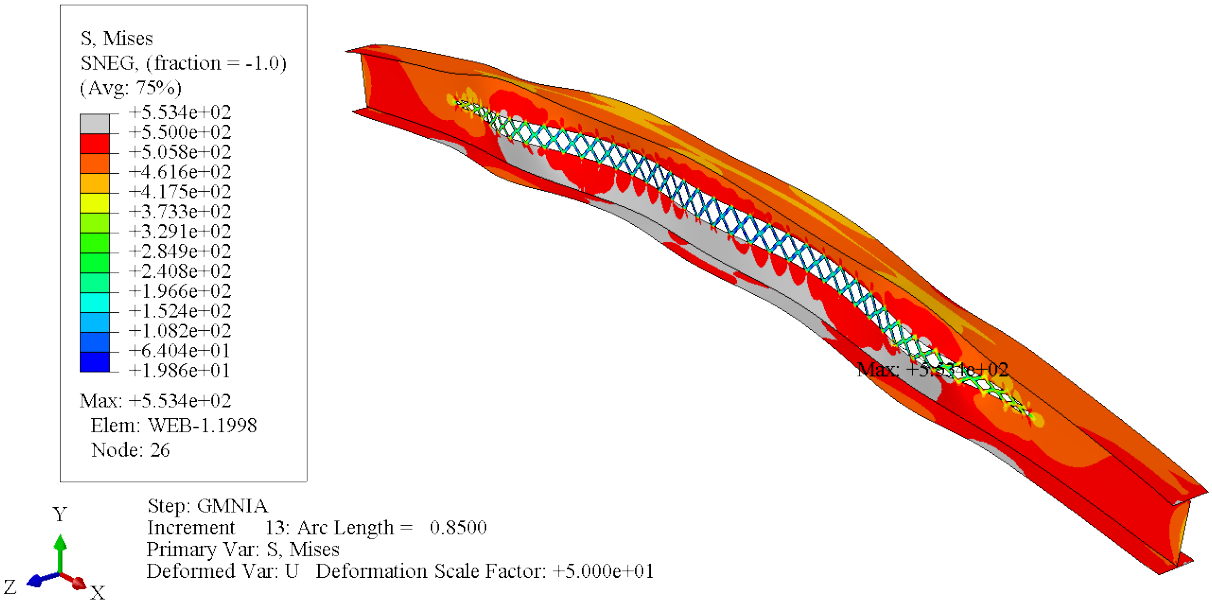

Figure 5.8: Von Mises stress plot at column collapse (model: 0.7-0.3-30-3.5)

The deformed shape and von Mises stress distribution in the column with maximum collapse load are presented in **Figure 5.8** above. Compared with the CHR opening models, the plastic hinge spread more uniformly in the central area of the web section on the compression side. It indicates that a more typical global buckling failure was achieved with nearly full utilisation of the web section at the bottom. Then, the figures in **Figure 5.9** clearly show the development of plastic hinges and failure mode under axial load. Similar to **Figure 5.4**, the colour from blue to red indicates the augment in stress magnitude, bounded by the maximum and minimum stresses shown in the figures.

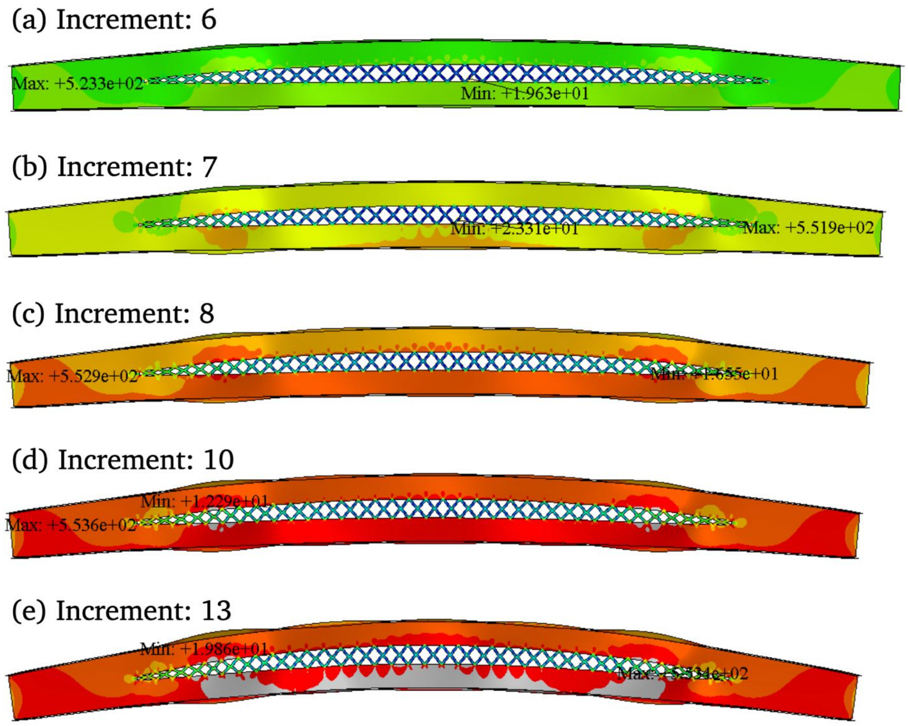

Figure 5.9: History of von Mises stress plot of model: 0.7-0.3-30-3.5 (unit: N/mm^2)

It can be seen in **Figure 5.9** that the geometric discontinuity induced stress concentration issue was mitigated by introducing this tapered opening pattern. But, the two smaller plastic hinges formed adjacent to the central one means the local instability issue still arose here, although the location of local buckling shifted towards the middle. In **Figure 5.9(d)** and **5.9(e)**, it could be confirmed that the local buckling induced yielding occurs in increment 10, then followed by a global buckling failure in increment 13, indicating that the local buckling still dominates the column failure and reduces the maximum resistance.

Therefore, judging from the above-mentioned facts, it can be concluded that for the 375 combinations investigated in this research, the global buckling interacted with the local buckling mode causes the column failure with the tapered opening which results in a loss of collapse load compared with the column with a solid web. The final solution of column with the tapered opening that has the maximum resistance of 277.68 kN is illustrated in **Figure 5.10** below.

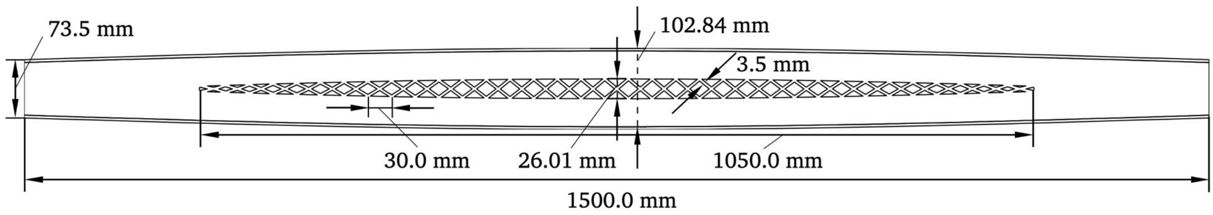

Figure 5.10: Layout of the strongest column with the tapered web opening

Furthermore, to investigate the relationship between resistance reduction and cross-section properties, the results from FE analysis were normalised by the compression capacity at the weakest section, expressed by **Equation 5.1**.

$$\rho = \frac{N_{u,FE}}{A_{min} f_y} \tag{5.1}$$

Where,

$N_{u,FE}$ is the collapse load from FE analysis.

A_{min} is the minimum cross-sectional area.

f_y is the yielding strength of WAAM S550 carbon steel, $f_y = 550.0$ N/mm²

Then, the relative slenderness, $\bar{\lambda}$, and cross-section slenderness, $\bar{\lambda}_p$, are calculated by **Equation 5.2** and **5.3**, respectively.

$$\bar{\lambda} = \sqrt{\frac{A_{min} f_y}{N_{cr,g}}} \tag{5.2}$$

$$\bar{\lambda}_p = \sqrt{\frac{A_{min} f_y}{N_{cr,l}}} \tag{5.3}$$

Where,

A_{min} is the minimum cross-sectional area.

f_y is the yielding strength of WAAM S550 carbon steel, $f_y = 550.0$ N/mm²

$N_{cr,g}$ is the eigenvalue of lowest global buckling mode from LBA.

$N_{cr,l}$ is the eigenvalue of lowest local buckling mode from LBA.

Hence, the normalised FE results are plotted against relative and cross-section slenderness for all 225 models as shown in **Figure 5.11**.

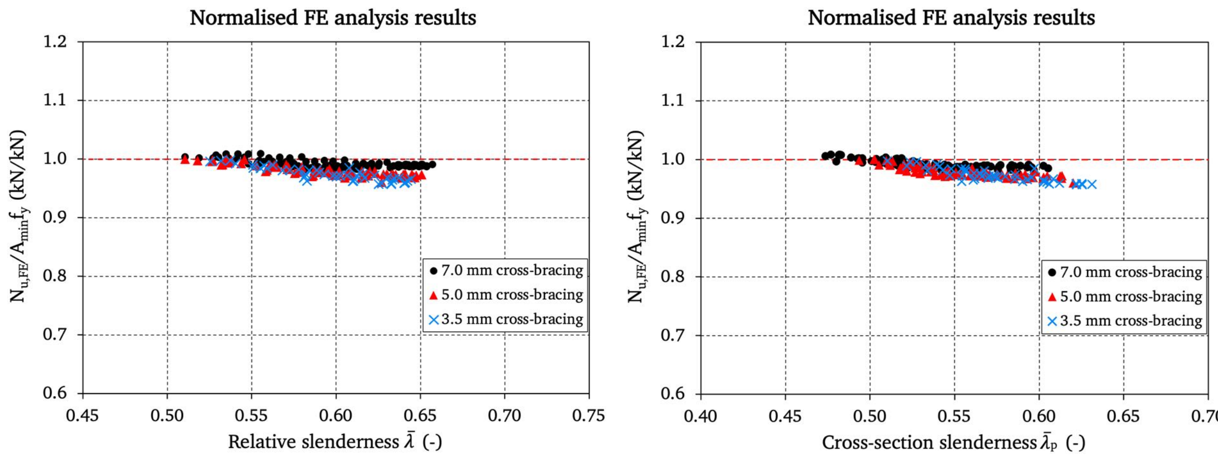

(a) (b)

Figure 5.11: Normalised FE analysis results against (a) relative slenderness and (b) cross-section slenderness

In this research, the value of slenderness did not vary much, because all the columns investigated have the same critical length and volume, and the materials removed are placed in web along the outer edges which gives the similar minimum cross-section areas.

As indicated in **Figure 5.11**, the same trend in resistance variation could be observed for relative and cross-section slenderness, where the reduction in column resistance is more pronounced as slenderness becomes greater. Although the interaction of local and global buckling dominates the column failure, the strength reduction due to buckling is less significant, where all of the ratios ($N_{u,FE}/A_{min}f_y$) exceed 0.9. Moreover, for both relative and cross-section slenderness, the wider cross-bracing gives a smaller reduction, which means that with the 7.0 mm bracing, the column is less sensitive to global and local buckling. In this case, the material failure is more pronounced in the failure mode interaction, but the local and global buckling still play the leading roles.

The minimum area used in slenderness calculation also provides insight into the impacts of the opening dimension on the resistance reduction, which will be involved in the next section.

5.2.3 Impact of different tapered opening and cross-bracing dimensions

With regard to the impact of various opening and bracing dimensions on the column resistance, **Table 5.3**, above shows a similar trend concerning maximum resistance variation with different opening heights as that observed in CHR web opening optimisation. For models with all bracing widths investigated, the column collapse loads degrade significantly with greater opening height. Therefore, to further explore the impacts of length of opening, spacing and width of cross-bracing on the column resistance, all 225 data points from FE analysis are classified by cross-bracing width and put in three 3D spaces. Then, in each 3D space, five surfaces are obtained based on the data points with the same opening height by using surface linear interpolation in MATLAB (The MathWorks, 2022). Therefore, the X- and Y-coordinate could be labelled as opening length and bracing spacing, with the maximum resistance in Z-coordinate. In this way, all data points with four variables could be included in only three 3D plots as presented in **Figure 5.12**, **5.13** and **5.14** as follows.

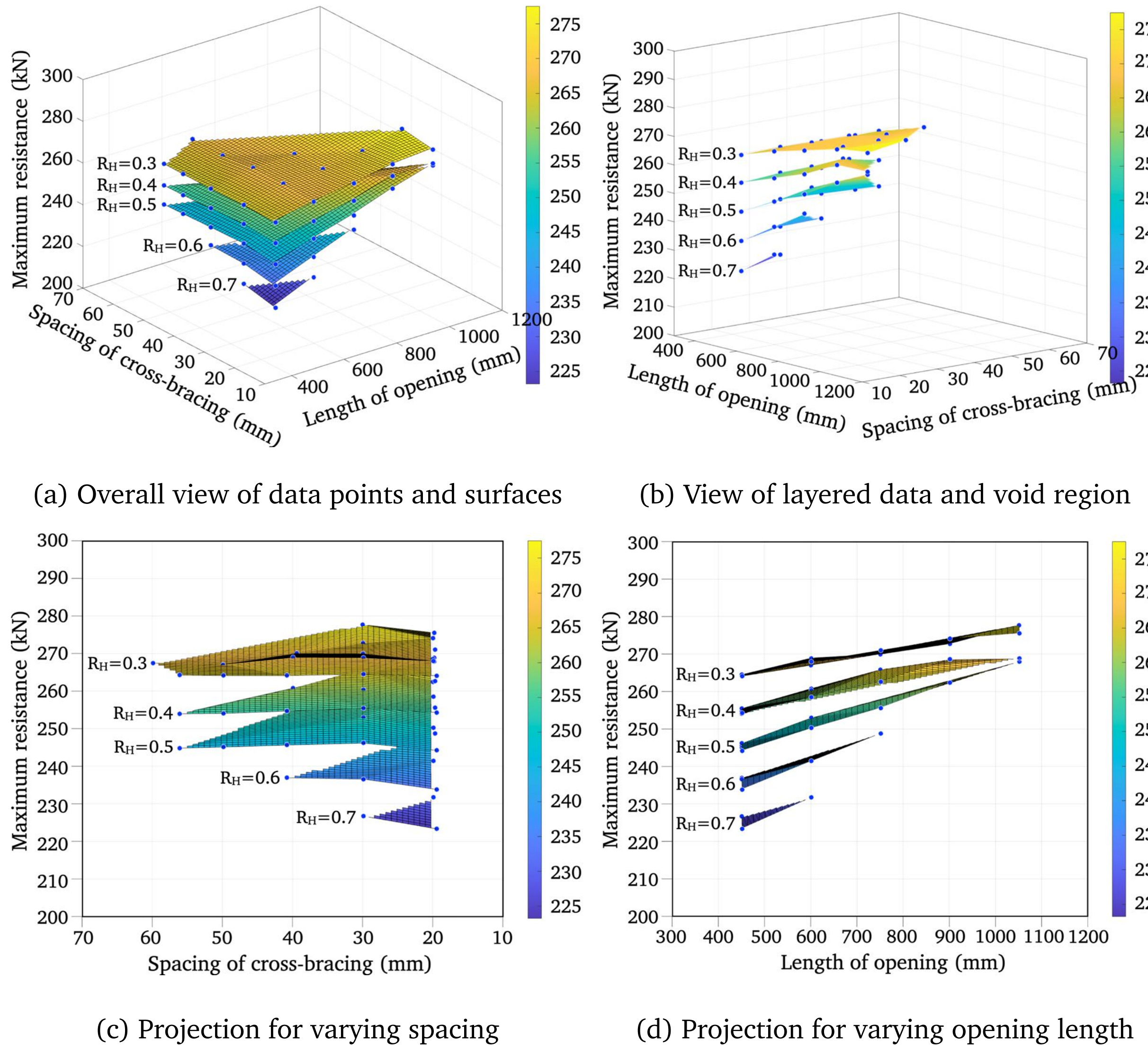

(a) Overall view of data points and surfaces

(b) View of layered data and void region

(c) Projection for varying spacing

(d) Projection for varying opening length

Figure 5.12: 3D Plot of P_{max} results based on 3.5 mm cross-bracing models

In this case, only the columns with the major axis buckling in the lowest eigenmode are included, as shown in **Figure 5.12(a)** and **5.12(b)**. According to the combinations defined, every surface should have a rectangular projection in the XY-plane. However, for 3.5 mm width bracing models, all five surfaces with varying opening heights are not full surfaces. This is because some data points are dropped due to unexpected local buckling mode.

If the data points at truncated edges are connected on all surfaces, a new surface boundary could be obtained, serving as the boundary between local buckling and global buckling for all combinations, which could be called “local buckling surface”. Apparently, this surface will shrink with the increase in cross-bracing width, which will be introduced later.

Regarding the varying bracing spacing in 3.5 mm width bracing models, no noticeable variation could be observed in column resistances, except for the slight drop when spacing reaches 20.0 mm. This is due to the different web size after amplitude modification, where the 20.0 mm spaced cross-bracing gave a quite dense truss pattern in the opening which reduced the amount of material removed. In this way, the web width after amplitude modification was less than those with the larger spacing of bracings. Although the 20.0 mm spacing benefits the local buckling control and outstand T-section stabilisation, the effects of decreasing web width on collapse load reduction are more pronounced.

In **Figure 5.12(d)**, a rising trend in column maximum resistance could be witnessed for each height ratio, confirming that the increasing opening length has a positive impact on improving the column capacity. This is attributed to the increment in the second moment of area at mid-length cross-section, which effectively improves the column resistance to global buckling dominated failure. Although the increment in opening length benefits the column capacity, the opening dimension was constrained within 1050.0 mm, to avoid the disturbance of the highly stressed region near ends observed in benchmark column.

The same series of plots is also created for models with 5.0 mm cross-bracings as presented in **Figure 5.13** on the next page.

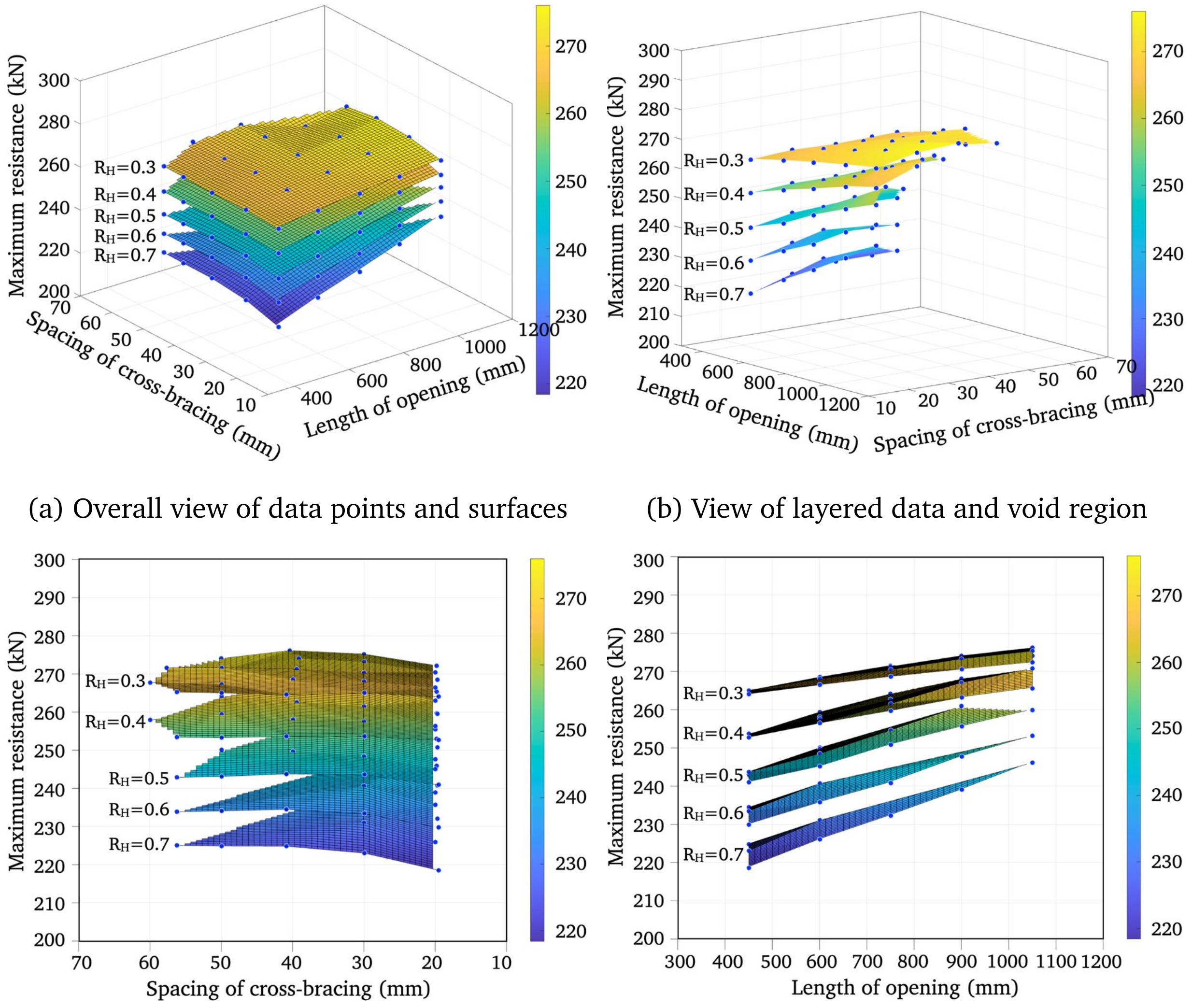

(a) Overall view of data points and surfaces

(b) View of layered data and void region

(c) Projection for varying spacing

(d) Projection for varying opening length

Figure 5.13: 3D Plot of P_{max} results based on 5.0 mm cross-bracing models

Compared with the 3.5 mm bracing models, larger data surfaces are obtained from 5.0 mm bracing models, which is because the stronger cross-bracing provides more stiffness in openings to resist local instabilities. Then, more data points are included in this case, and the "local buckling surface" shrinks towards the right hand side corner, as shown in **Figure 5.13(b)**, representing the combination of greater bracing spacing and opening length.

With regard to the impact of different spacing for 5.0 mm bracings, the trend is similar to that mentioned for 3.5 mm bracing models. But, the degrading of collapse load is more obvious in this case, since the 5.0 mm bracing will take up more space when the cross-bracings become closer to each other. As for the varying opening length, exactly the same trend is captured as that from 3.5 mm bracing models, as shown in **Figure 5.12(d)** and **5.13(d)**, where the growing opening length leads to a higher column capacity.

Furthermore, the same graphs are created for 7.0 mm bracing models as well in **Figure 5.14**, to investigate the impacts of different opening lengths and spacings on column resistance in all 7.0 mm bracing models.

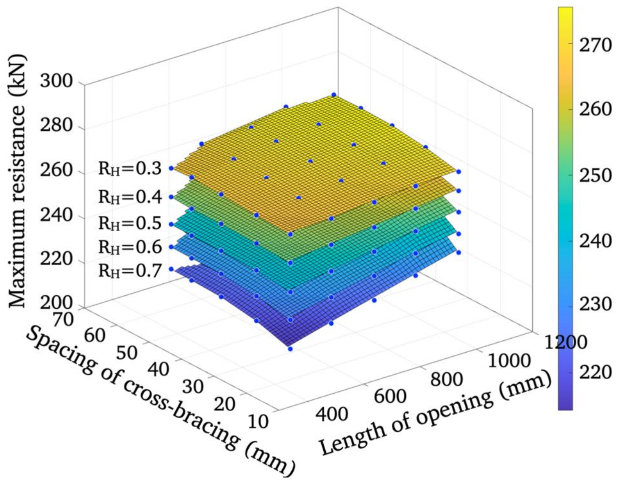

(a) Overall view of data points and surfaces

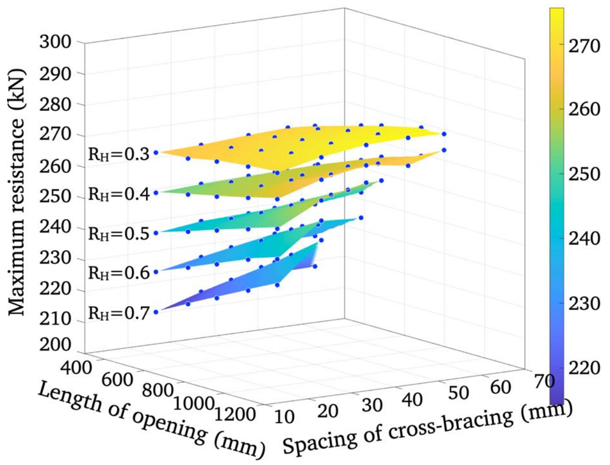

(b) View of layered data and void region

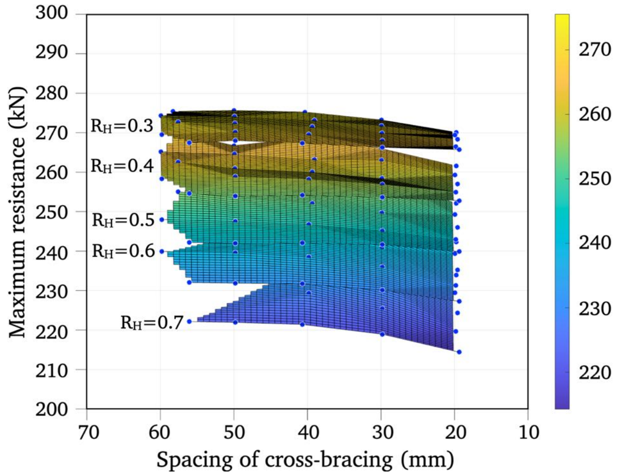

(c) Projection for varying spacing

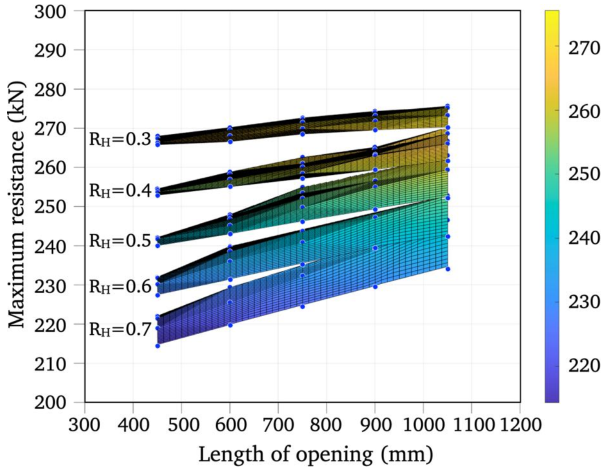

(d) Projection for varying opening length

Figure 5.14: 3D Plot of P_{max} results based on 7.0 mm cross-bracing models

With the stabilisation provided by the 7.0 mm width cross-bracings, more data points are involved in this plot, where only the surfaces with height ratios of 0.5, 0.6 and 0.7 are truncated, attesting that the "local buckling surface" continues to shrink compared with 3.5 mm and 5.0 mm bracing models. It could be predicted that when the bracing width rises to a certain value that is large enough, no data points will be abandoned due to the local buckling mode for columns with the same volume and initial height.

Last but not least, the same trends could be found for the varying spacing and opening length as those in both the 3.5 mm and 5.0 mm bracing models, where the only difference is the reduction of collapse load presents a moderate upward tendency with the rise of cross-bracing width which could be inspected in **Figure 5.12(c)**, **5.13(c)** and **5.14(c)**.

5.2.4 Summary

In this section, the results of FE analysis for all 225 column models with tapered opening were delivered, followed by the analysis concerning the impact of varying opening and cross-bracing dimensions on the collapse loads.

Due to the interaction of local buckling and major axis global buckling, the maximum column collapse loads of all 225 column models within these parametric studies was 277.68 kN, less than that of the reference column with varying cross-sections, where a 3.2% reduction was obtained.

Moreover, the surface fitting in MATLAB was employed to present the data points in a 3D space for each cross-bracing width, based on which the impacts of various opening and bracing dimensions were analysed. The volume of the void region, representing models with local buckling below the "local buckling surface", dropped with the rise in cross-bracing width, since the stability of outstand web sections was enhanced. Furthermore, it can be concluded that with the same volume and initial height, the higher collapse load could be achieved by slightly enlarging the spacing of braces or creating a long narrow web opening.

The parametric studies conducted herein showed a constraint that there is no significant difference between opening patterns, with the variation in opening and bracing dimensions leading to the same failure mode. So, finding a flexible opening pattern to mitigate the interaction of local and global buckling modes becomes very difficult. Therefore, the topology optimisation was further employed to investigate the optimum design of this I-section column with web openings, as presented in **Section 5.3**.

5.3 Nonlinear topology optimisation

5.3.1 TO model introduction

In terms of the topology optimisation, the effects of volume fraction and material interpolation penalty factor were investigated in this column optimisation research. In total, 35 combinations connecting these two parameters were involved as summarised in **Table 5.4**.

Table 5.4: Parameters investigated in topology optimisation

Index	Volume fraction (VF)	Penalty factor (PF)
1	0.60	3.0
2	0.65	4.0
3	0.70	5.0
4	0.75	6.0
5	0.80	7.0
6	—	8.0
7	—	9.0

As introduced before, the volume fraction was defined as a constraint for algorithm to be achieved during the optimisation iterations. If the convergence in TO could be achieved, the normalised mass distribution tends to result in solid structures in the computing domain having 1.0 density, while other void regions will have zero density. In this particular case, the volume fraction will then be the ratio of volume of solid structures to the whole computing domain.

Furthermore, the material interpolation factor is the order of the power function describing the relationship between stiffness and material density, as shown in **Figure 5.15**. The recommended power for the interpolation function should be greater than 3 to achieve the density of zero or one everywhere within the computation domain (Bendsøe & Sigmund, 1999). It means the higher order power functions are needed to reduce the stiffness of material with low density to realise a true “0-1” structure scheme. Hence, the primary investigation group included the PF from recommended 3 to 9, to show the impacts of the various powers of interpolation function on the TO convergence.

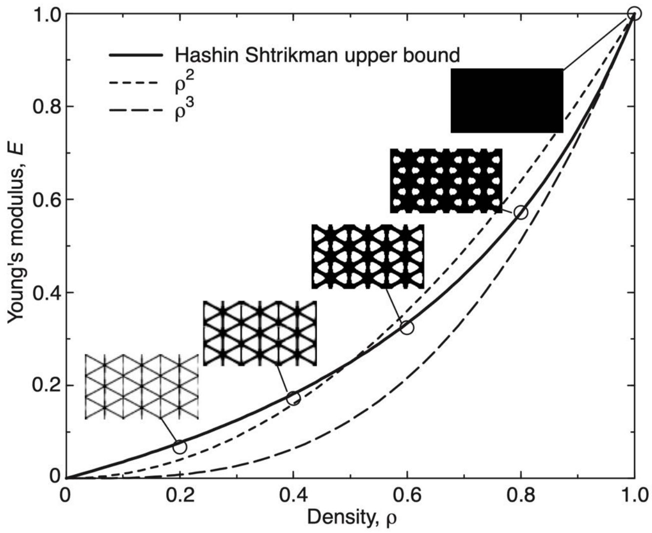

Figure 5.15: Material interpolation in SIMP (Bendsøe & Sigmund, 1999:p.640)

5.3.2 Results of mass density from TO

The nonlinear topology optimisation was conducted for all 35 combinations following the methodology in **Chapter 3**, where the minimising the maximum displacement in transverse direction was defined as the objective function with the volume fraction in web serving as the constraint. As illustrated in **Figure 5.16**, the density contour graphs for all columns have the convergence issues, where the "0-1" density layout was not well achieved, where the density exceeded 0.3 in most of the area within the computation domain. Therefore, among all the combinations, only three models with comparatively reasonable mass density solutions were presented herein.

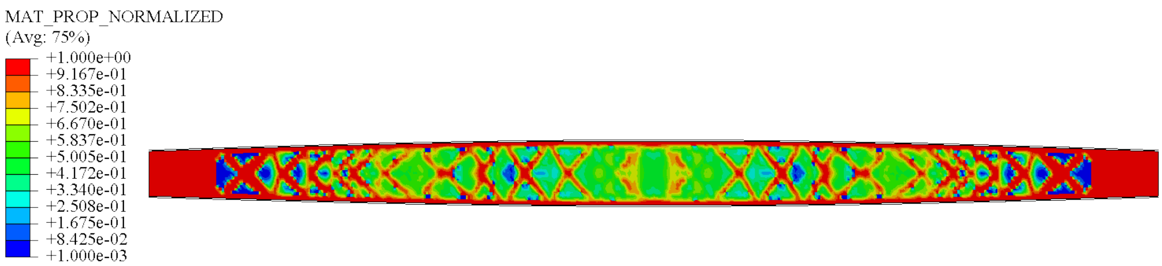

(a) Volume fraction: 0.7 and penalty factor: 4.0

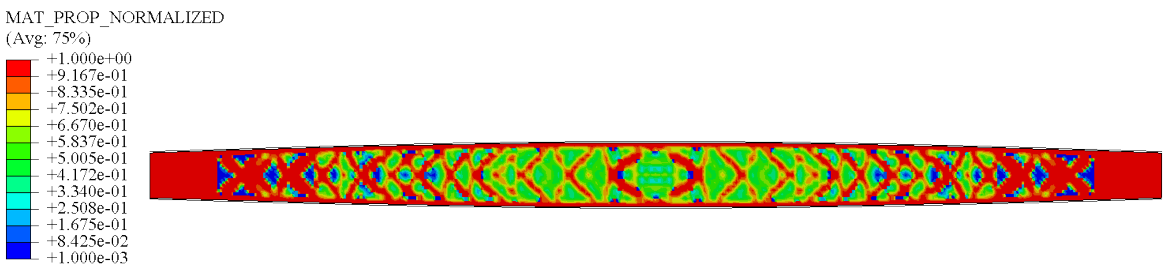

(b) Volume fraction: 0.75 and penalty factor: 4.0

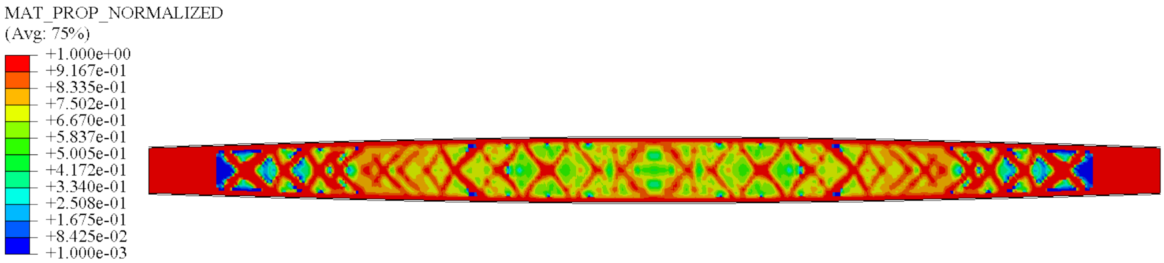

(c) Volume fraction: 0.8 and penalty factor: 8.0

Figure 5.16: Three mass density solutions from TO

In the material density plots, the red zones indicate the solid material whose density approaches one, whilst the blue zones represent the locations, in which the material could be removed due to the zero density. Additionally, the green and yellow zones represent transition regions, where intermediate material density could be found.

The recommended volume fractions are 0.7, 0.75 and 0.8, since the materials in this varying cross-section column have already been mostly utilised, and there is not much material that could be removed without introducing stability issues. It could be observed in **Figure 5.16** that all the solutions from TO are complex cross-bracings connecting the flanges, under the combination of bending and axial compression. The double symmetry constraints defined in topology optimisation could provide sufficient flexural stiffness in both directions, which settles the problem of uncertain bending direction for columns under compression. Furthermore, less solid materials are placed near the mid-length position, where the bending effects is predominate. And, it appears that the solid materials concentrate at the quarter places near the ends, due to the interaction of the secondary bending moment and axial compression. At these locations, the materials on both the outer surfaces and neutral axis are utilised more efficiently.

5.3.3 Results of collapse load from GMNIA

In this case, considering that the convergence of TO was not well realised, the appropriate density value will be taken to create openings, accompanied with full filtering function in ABAQUS to generate the geometry for further analysis. The following **Figure 5.17** shows the geometries extracted from ABAQUS, in which the floating materials and small outstand parts were trimmed to get smooth opening patterns. These three geometries were employed in the LBA and GMNIA to plot the load-deformation curves, based on which the collapse loads were obtained.

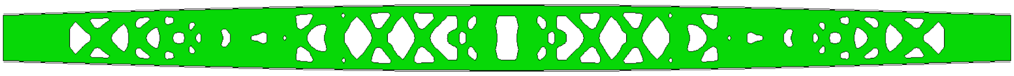

(a) Volume fraction: 0.7 and penalty factor: 4.0 (density: 0.503)

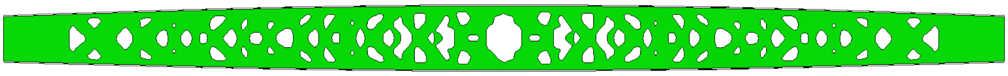

(b) Volume fraction: 0.75 and penalty factor: 4.0 (density: 0.594)

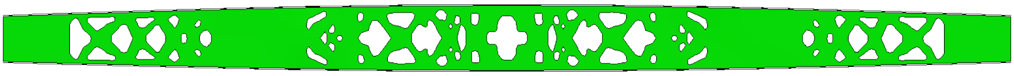

(c) Volume fraction: 0.8 and penalty factor: 8.0 (density: 0.620)

Figure 5.17: Geometrically defined surfaces from TO

Thereafter, the LBA and GMNIA were performed, following the procedures introduced before, and the plots of load-deformation curve are presented in **Figure 5.18**.

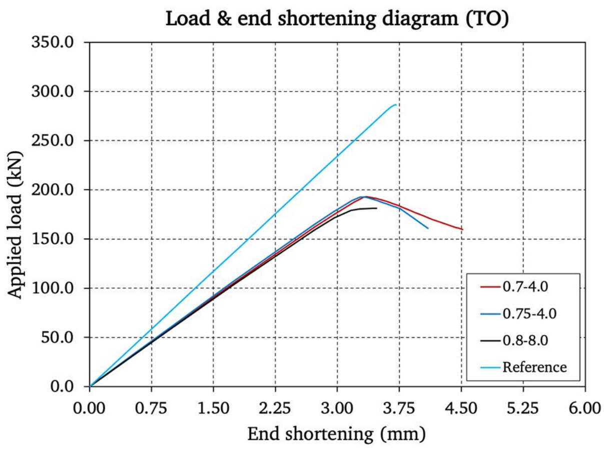

(a) Load-end shortening curves

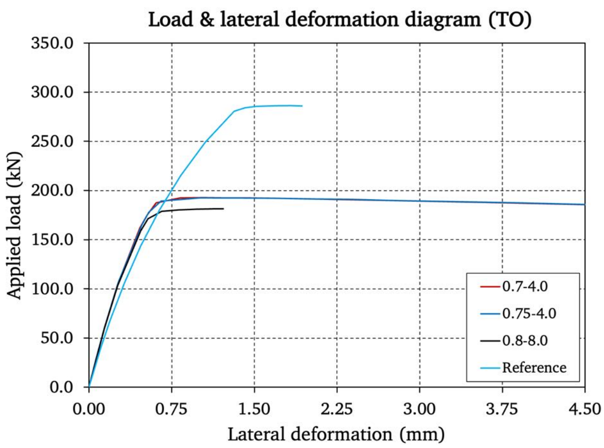

(b) Load-lateral deformation curves

Figure 5.18: Load-deformation curves for selected TO models

The failure modes of TO models with 0.7 and 0.75 volume fractions are dominated by major axis buckling, whilst the 0.8 VF model failed mainly due to the squashing failure, characterised by a plateau after the linear region in load-end shortening curve. It is clearly shown that all the collapse loads of TO models are less than that of the reference column. But, considering that the volumes of TO models were changed during geometry extraction, the maximum resistance should be normalised and then compared with the reference value.

In **Table 5.5**, all the normalised P_{max} are calculated and listed along with the model information from topology optimisation.

Table 5.5: Summary of maximum resistance for columns from TO

Index	VF (-)	PF (-)	Mass density for extraction	Volume (mm^3)	Volume ratio (V/V_{ref})	Normalised P_{max} (kN)	δ_{ref}
1	0.7	4.0	0.503	767467.56	0.93	207.25	-27.8%
2	0.75	4.0	0.594	781495.38	0.95	203.20	-29.2%
3	0.8	8.0	0.620	772758.38	0.94	193.64	-32.5%

After normalisation, the maximum resistance of column modelled by TO are still less than that of the reference column, where the minimum loss is 27.8%. The potential reasons for this capacity loss could be analysed based on the von Mises plots at failures when the P_{max} was obtained, as shown in **Figure 5.19**.

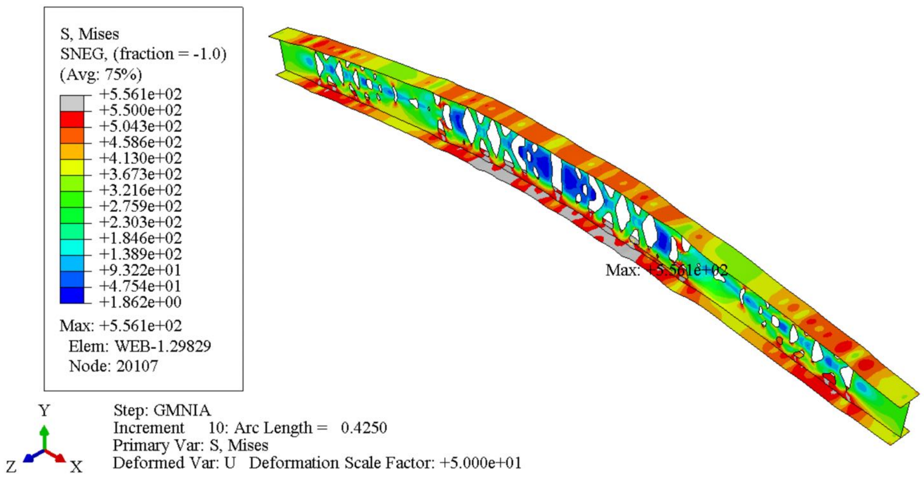

(a) Volume fraction: 0.7 and penalty factor: 4.0

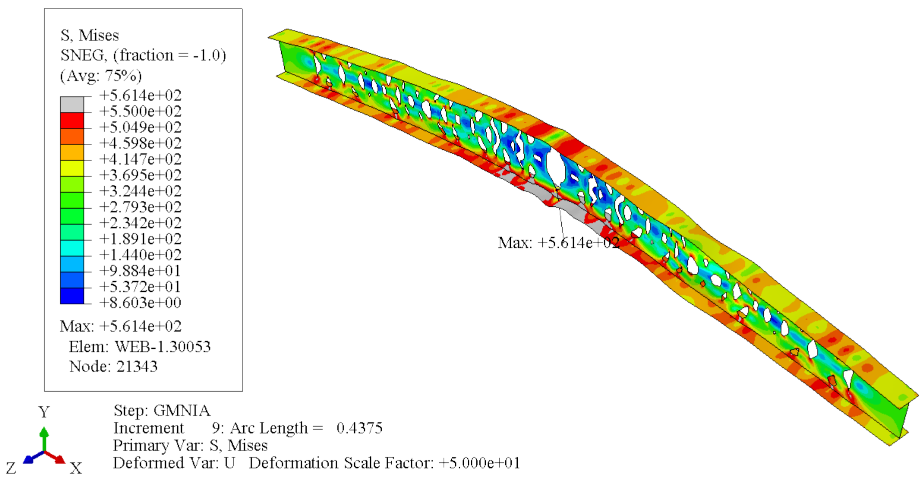

(b) Volume fraction: 0.75 and penalty factor: 4.0

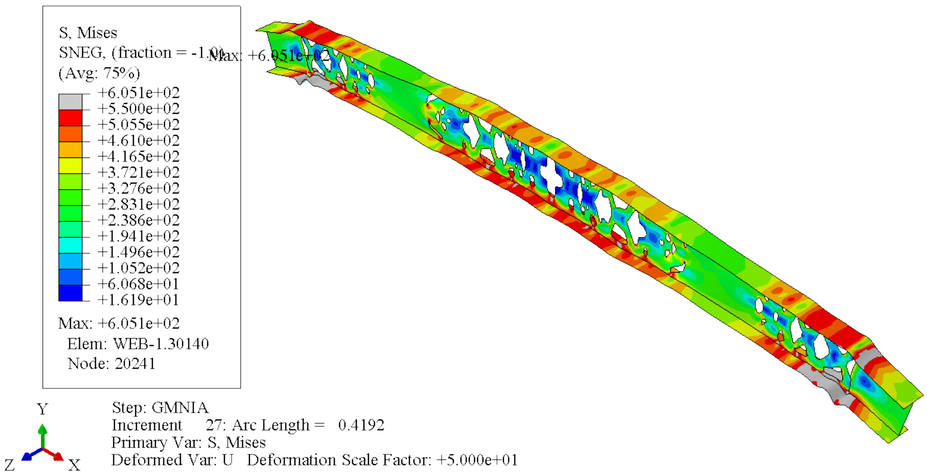

(c) Volume fraction: 0.8 and penalty factor: 8.0

Figure 5.19: Von Mises stress plot at column collapse for selected TO models

For models in **Figure 5.19(a)** and **5.19(b)**, the plastic hinges locate at the middle of the column, presenting an obvious global buckling failure mode, whilst the plastic hinges in column **5.19(c)** are formed at the ends of the column, which allow the rotations mainly occur at ends. Hence, the predominant material failure mode could be identified, which has good agreement with the conclusion from the load-deformation curve. The squashing failure indicated that too much material was removed at column ends, making it less stiff compared with the middle region.

In terms of the buckling failure dominated models, the local imperfection did not have obvious effects; rather, the shallow T-section at the middle opening became the critical section, where the secondary bending was significant. Hence, the materials should be retained in the middle region to provide sufficient flexural stiffness against global buckling. Then, a new frozen area in TO was proposed in the web section to further explore the optimum opening schemes in the column web.

5.3.4 Further investigation in TO with mid-length connection

Based on the previous TO model, a 10.0 mm wide post at the middle was added to the frozen area to prevent the materials being removed in the central region, which helped stabilise the flanges and T-sections. The general layout of the frozen region in updated TO models is shown in **Figure 5.20**.

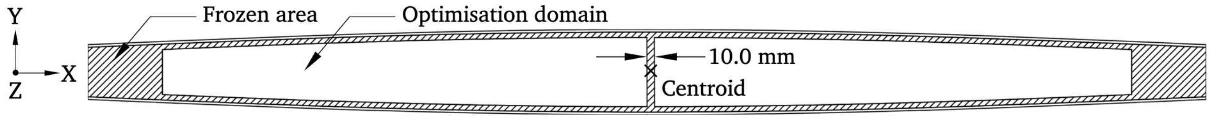

Figure 5.20: General layout of column TO model with mid-length post

The shaded region represents the frozen area, in which the full density solid section will be created during iterations in TO, similar to the layout introduced earlier. Furthermore, according to the TO carried out in the last section, the average volume ratio was approximately 0.94, which was employed to increase the volume in advance to approach the reference value after TO. Moreover, the same combinations for volume fraction and penalty factor as shown in **Table 5.4** were investigated, and the results are presented in **Section 5.3.5** and **5.3.6**.

5.3.5 Results of mass density with mid-length post

Among all the solutions, three typical models were selected herein with the same volume fractions as those involved in the last TO, but the penalty factors were different in this case, as shown in **Figure 5.21**.

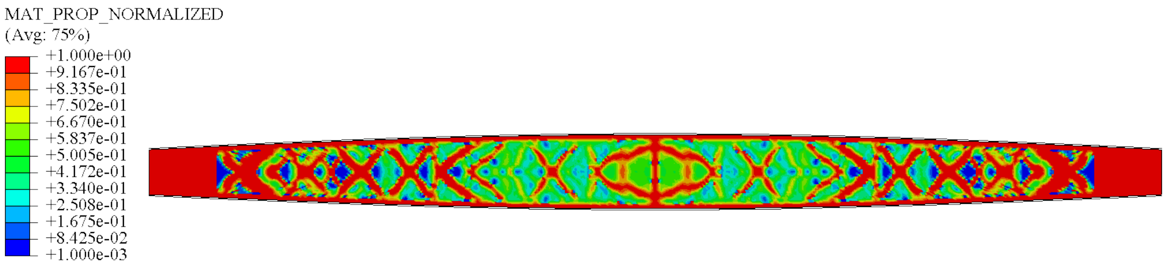

(a) Volume fraction: 0.7 and penalty factor: 3.0

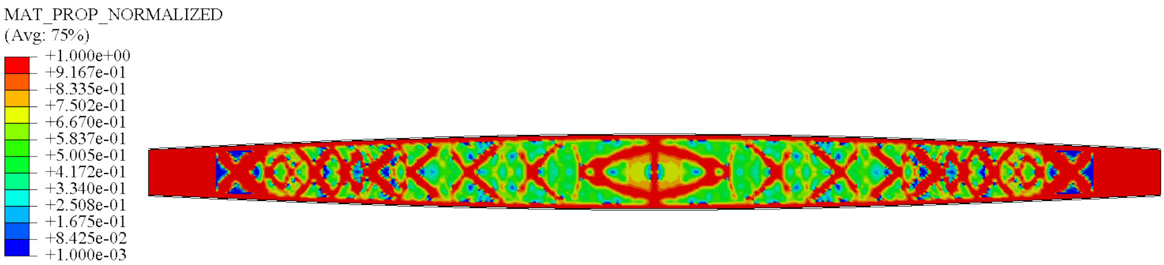

(b) Volume fraction: 0.75 and penalty factor: 4.0

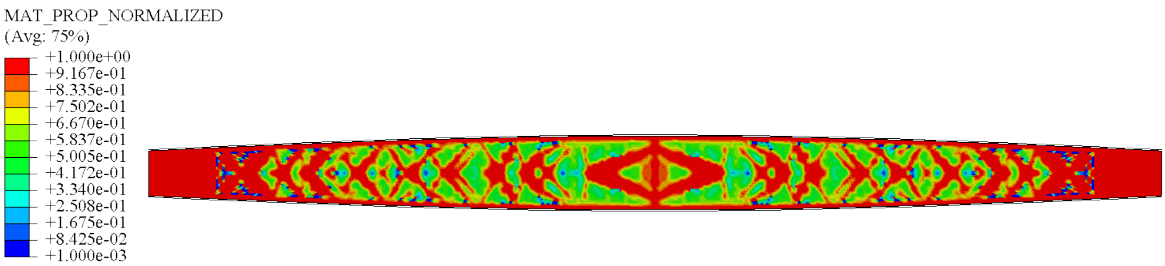

(c) Volume fraction: 0.8 and penalty factor: 4.0

Figure 5.21: Three mass density solutions from models with mid-length post

In TO models with middle posts, the cross-bracings connecting the flanges are more rationally designed, and a low density region can be observed in the middle, where shear forces are relatively low. The updated TO models still have the convergence problem, since most of the web remains in yellow and green with a mass density greater than 0.3.

5.3.6 Results of collapse load from GMNIA (with mid-length post)

Based on the mass density distribution, the new geometries were extracted with the reasonable mass densities to ensure the effective connection between flanges. As shown in following **Figure 5.22**, the side view of the geometries with mid-length post are delivered. The volume fraction, penalty factor and extraction density are provided along with each geometry.

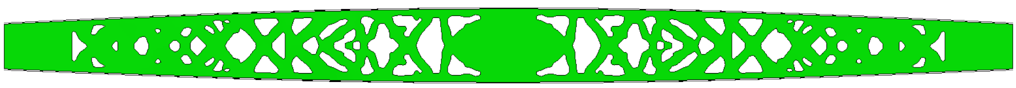

(a) Volume fraction: 0.7 and penalty factor: 4.0 (density: 0.471)

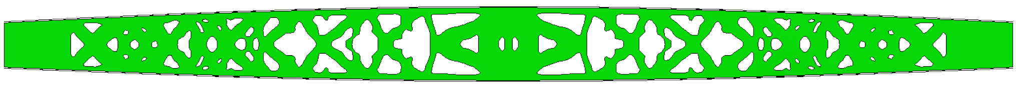

(b) Volume fraction: 0.75 and penalty factor: 4.0 (density: 0.570)

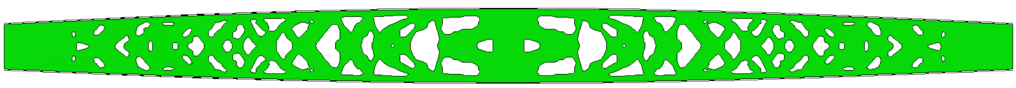

(c) Volume fraction: 0.8 and penalty factor: 8.0 (density: 0.612)

Figure 5.22: Geometrically defined surfaces for models with mid-length post

Then, with the new TO geometries, the LBA and GMNIA were conducted in ABAQUS, and the load-deformation curves could be found in **Figure 5.23** as follows.

In this case, the failure mode of all three TO models are dominated by the global buckling, interacted with local buckling at T-sections. None of these TO models has a greater maximum resistance than the reference column under axial compression. Taking the volume difference into account, the normalised maximum resistances for all models are calculated as presented in **Table 5.6** in the next page.

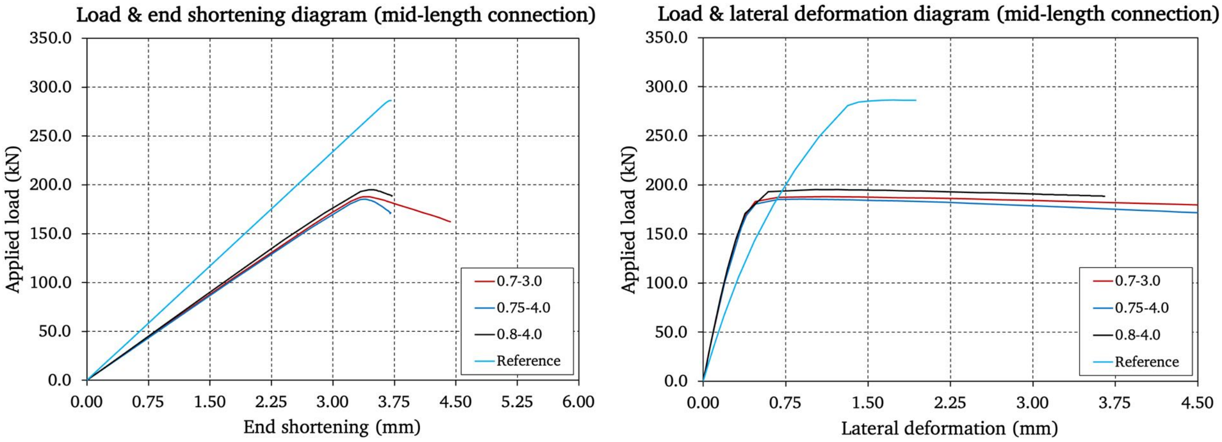

(a) Load-end shortening curves (b) Load-lateral deformation curves

Figure 5.23: Load-deformation curves for selected TO models with middle post

Table 5.6: Summary of maximum resistance for columns with mid-length post

Index	VF (-)	PF (-)	Mass density for extraction	Volume (mm³)	Volume ratio (V/V_{ref})	Normalised P_{max} (kN)	δ_{ref}
1	0.7	3.0	0.471	796520.25	0.97	194.57	-32.2%
2	0.75	4.0	0.570	784038.94	0.95	195.12	-32.0%
3	0.8	4.0	0.612	803507.88	0.97	200.28	-30.2%

As shown in **Table 5.6**, the losses of resistance are greater than 30% for all three TO models with a mid-length post, which are even worse than the topology optimised models without the post. The reason for this phenomena could be further explored based on the von Mises plots at collapse as shown in **Figure 5.24**.

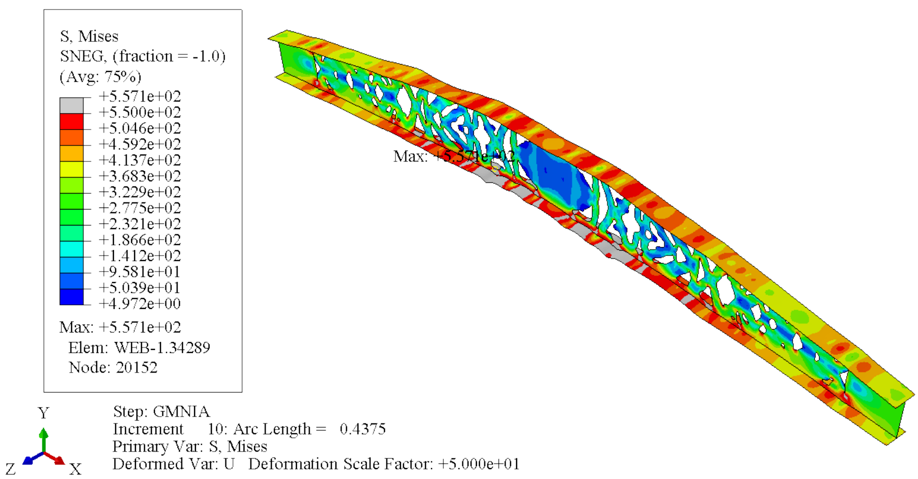

(a) Volume fraction: 0.7 and penalty factor: 3.0

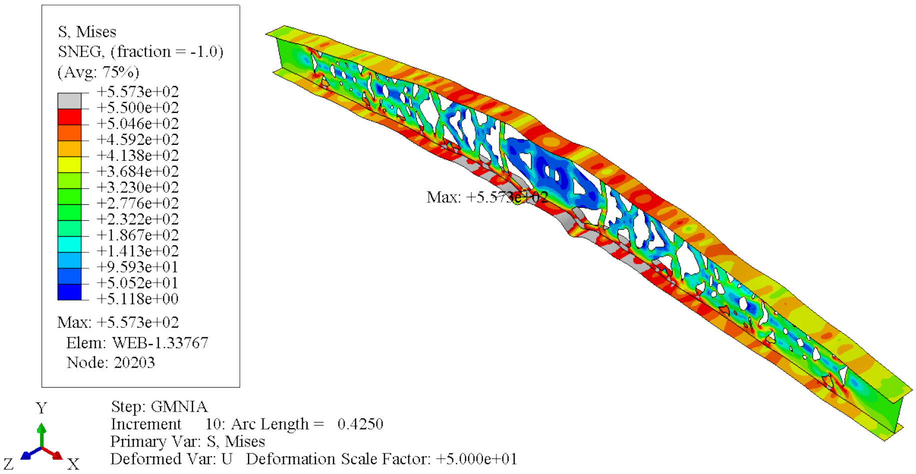

(b) Volume fraction: 0.75 and penalty factor: 4.0

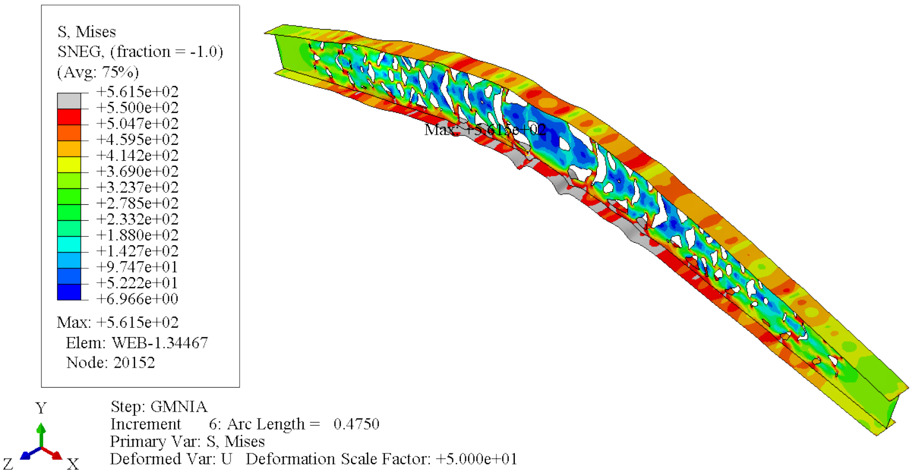

(c) Volume fraction: 0.8 and penalty factor: 4.0

Figure 5.24: Von Mises stress plot at column collapse for TO models with middle post

As indicated in **Figure 5.24**, the T-sections in the middle of the column suffered from the local buckling firstly and lost strength which led to the global buckling afterwards. This issue also occurred in the TO models without the mid-length post, indicating that the TO solutions in the study tend to create some shallow T-sections which are easily prone to the local instability problem. The potential reason for this problem could be explained by the method employed in imperfection definition in FE model. The objective function defined was to minimise the lateral deformation by improving the flexural stiffness, where the buckling issues were only related to the convergence of analysis step defined in ABAQUS.

Furthermore, although the nonlinear topology optimisation was conducted, the perfect mesh with only global imperfection (triggered by a lateral load) could not account for the local bucking issue at T-sections during the analysis. So, the performance of topology optimised structures in the LBA and GMNIA is not as good as expected due to the local buckling problem.

Therefore, for the topology optimisation of thin-walled members, both the global and local buckling should be taken into account during the iterations for material interpolation to obtain the solid structures with high buckling resistance as well. To address this problem, the lowest global and local eigenmodes could be assigned as mesh perturbations in the Static General step employed in topology optimisation in ABAQUS.

Chapter 6 — Conclusion

6.1 Achievements

By employing the FE analysis package ABAQUS, the numerical study into the optimisation of thin-walled steel I-section columns was conducted in this research. For slender columns subject to compression with secondary bending moment, the fibres at outer surfaces usually are effectively utilised, whilst those inside the column are lightly stressed during loading. Consequently, web openings in columns may be considered as a viable option to make better use of the materials in columns and achieve better structural performance.

Hence, the optimisations in this study focused on the creation of web openings with cross-bracings and redistribution of materials to where needed, to improve the maximum column resistance to axial compression. The displacement-controlled axial load was employed, accompanied by the global and local imperfections to trigger the secondary bending effect. Besides, the interpolated WAAM S550 material properties were adopted due to the lack of material experiment data.

Based on the validated FE models, the parametric studies were systematically carried out, including various web opening and cross-bracing dimensions for both constant height ratio opening and tapered opening. Then, the nonlinear topology optimisation was performed as well to explore the capability of the TO algorithm in obtaining a higher resistance of the column under compression.

In total, 750 FE models were established, using the FE analysis package ABAQUS with Python scripts, within the parametric studies, with 375 models for each opening pattern, covering every combination of four parameters, namely the opening length, opening height, spacing and width of cross-bracing. The LBA was conducted for all models, whose output was used in checking the lowest buckling mode, based on which the GMNIA was performed for global buckling dominated columns only. Then, the optimum design of varying cross-section I-section columns and the impacts of various opening and bracing dimensions were investigated based on the collapse loads and load-deformation curves from GMNIA.

Furthermore, the nonlinear topology optimisation was conducted with different combinations of volume fractions and material penalty factors, including two layouts of the computational domain. The load-deformation curves and collapse loads were obtained from the LBA and

GMNIA as well, based on which the capacity of TO in geometry optimisation for columns under compression was explored.

6.2 Conclusions

In this study, the sinusoidal profile column with 73.5 mm initial height and 90.2 mm mid-height with 3.5 mm flange and web thickness was regarded as the benchmark that achieved a 286.90 kN resistance, based on which the optimisations with web openings were conducted.

Based upon the numerical parametric studies performed, the maximum resistance from the column with constant height ratio opening was 275.15 kN, attained from the opening pattern with 900.0 mm length and 26.01 mm height, braced by the 3.5 mm truss with a 50.0 mm spacing. The loss of strength was attributed to the stress concentration at the ends of web opening and local buckling at T-sections for columns with constant height ratio opening. Moreover, in terms of the column with tapered opening, the same combinations were employed, and the maximum resistance 277.68 kN was obtained from the opening with 1050.0 mm length and 26.01 mm height, braced by the 3.5 mm truss with a 30.0 mm spacing, where a 3.2% percentage drop was observed. Within this study, the global buckling interacted with the local buckling at T-sections dominated the column failure, due to the reduction in stiffness compared with the reference column.

Furthermore, the impacts of the various dimensions of the tapered opening and cross-bracing on the maximum resistance were explored based on the FE analysis results,. With the increasing bracing width, the void region below the "local buckling surface" shrank continuously towards the corner representing the greater opening length and bracing spacing. Besides, with the same volume and initial height, higher column resistance could be obtained by reducing the opening height as well as increasing the opening length and brace spacing.

Last but not least, an investigation into the nonlinear topology optimisation of the thin-walled steel I-section columns was also carried out herein. There were two computational domains investigated with different volume fractions and penalty factors. The maximum normalised resistance was 207.25 kN, from the TO model with frozen areas only at ends. By adding the mid-length post, the maximum resistance was reduced to 200.28 kN, resulting in the "unoptimised" columns as well. The reduction of resistance was primarily induced by the inconsistency of imperfections assigned in TO and GMNIA, due to which the local buckling at T-sections apparently deteriorated the column performance.

6.3 Limitations and future work

Due to the limitations of this study, the maximum resistances of columns in parametric studies and topology optimisation are below the benchmark value. To further investigate this optimisation problem, the detailed limitations in parametric studies and TO are summarised separately, as follows.

For parametric studies, the range of opening length, opening height and bracing spacing adopted should be widened, since the impacts on resistance concerning these three parameters all showed the monotonic trend, where further investigations could be carried out to find better solutions. Then, it is not necessary to employ more slender bracings in the future investigation, as the member size is limited to 3.5 mm by WAAM technique currently.

In terms of the topology optimisation, as mentioned in the last chapter, the imperfection introduced in TO models was only equivalent global imperfection by using lateral loads which have trouble triggering the local buckling effectively under the axial compression. To keep the consistency of the imperfections defined in TO models and GMNIA models, both the lowest global and local eigenmode imperfection could be utilised as mesh perturbations in topology optimisation to effectively capture the local buckling at T-sections in the future investigations.

References

Allaire, G., Jouve, F. & Toader, A. M. (2002) A level-set method for shape optimization. *Comptes Rendus Mathematique.* 334(12), 1125-1130.

ASTM International. (2015) ISO/ASTM 52900:2015(E) *Standard terminology for additive manufacturing technologies - general principles - terminology.* West Conshohocken: ASTM International.

Baker, R. (1925) *Method of making decorative articles*. United States Patent and Trademark Office US1533300A (Patent).

Bendsøe, M. P. (1989) Optimal Shape Design as a Material Distribution Problem. *Structural optimization.* 1(4), 193-202.

Bendsøe, M. P. & Sigmund, O. (1999) Material Interpolation Schemes in Topology Optimization. *Archive of applied mechanics.* 69(9), 635-654.

Berman, B. (2012) 3-D printing: The New Industrial Revolution. *Business horizons.* 55(2), 155-162.

Blanther, J. E. (1892). *Manufacture of Contour Relief Maps*. United States Patent and Trademark Office US473901A (Patent).

Blasius, H. (1914) Träger kleinster Durchbiegung und Stäbe größter Knickfestigkeit bei gegebenem Materialverbrauch. *Zeitschrift für Mathematik und Physik–Organ für angewandte Mathematik.* 62, 182-197.

Bletzinger, K. U. & Ramm, E. (2001) Structural Optimization and Form Finding of Light Weight Structures. *Computers & Structures.* 79(22-25), 2053-2062.

Bourdin, B. & Chambolle, A. (2003) Design-Dependent Loads in Topology Optimization. *ESAIM: Control, Optimisation and Calculus of Variations.* 9, 19-48.

British Standards Institution 2005. BS EN 1993-1-1: 2005: Eurocode 3: *Design of steel structures, Part 1-1: General rules and rules for buildings*. London: British Standards Institution.

Buchanan, C. & Gardner, L. (2019) Metal 3D Printing in Construction: A Review of Methods, Research, Applications, Opportunities and Challenges. *Engineering Structures.* 180(2), 332-348.

Chung, K. F., Liu, T. & Ko, A. (2001) Investigation on Vierendeel Mechanism in Steel Beams With Circular Web Openings. *Journal of Constructional Steel Research.* 57(5), 467-490.

Cilley, F. H. (1900) the Exact Design of Statically Indeterminate Frame Works. An Exposition of its Possibility, but Futility. *Transactions of the American Society of Civil Engineers.* 43(1), 353-407.

Clausen, T. (1851) Über die form architektonischer säulen. *Bull. cl., Physico Math. Acad. St Pétersbourg.* 9, 369-380.

Cox, S. J. & Overton, M. L. (1992) On the Optimal Design of Columns Against Buckling. *SIAM Journal on Mathematical Analysis.* 23(2), 287-325.

Das, S. (1998) Direct Selective Laser Sintering of High Performance Metals: Machine Design, Process Development and Process Control. Austin, The University of Texas at Austin.

Das, S., Bourell, D. L. & Babu, S. (2016) Metallic Materials for 3D Printing. *Mrs Bulletin.* 41(10), 729-741.

Dassault Systèmes Simulia Corporation. (2021). *ABAQUS* (Version 2021) [Software] Dassault Systèmes Simulia Corporation. https://www.3ds.com/products-services/simulia/.

Dassault Systèmes Simulia Corporation. (2014) *Abaqus Analysis User's Manual 6.14.* Providence, Rhode Island, Dassault Systèmes Simulia Corporation.

DiMatteo, P. L. (1976). *Method of Generating and Constructing Three-Dimensional Bodies*. United States Patent and Trademark Office US3932923A (Patent).

Duque, M. (2022) *Design and Modelling of Thin-Walled I Columns with Variable Cross-section*. Undergraduate thesis. Imperial College London.

Durif, S. & Bouchair, A. (2016) Analytical Model To Predict the Resistance of Cellular Beams With Sinusoidal Openings. *Journal of Constructional Steel Research.* 121(6), 80-96.

Dutta, B. (2022) Directed Energy Deposition (DED) Technology. *Encyclopedia of Materials: Metals and Alloys*. 3, 66-84. doi:10.1016/B978-0-12-819726-4.00035-1.

El-Adly, S., Serror, M. & Hassan, A. (2011) Assessment for Local Buckling Coefficient of I-Section Web Under Uniform Compression. *Journal of Engineering and Applied Science.* 58(5), 403-415.

El-Sawy, K. M., Sweedan, A. M. & Martini, M. I. (2009) Major-Axis Elastic Buckling of Axially Loaded Castellated Steel Columns. *Thin-Walled Structures.* 47(11), 1295-1304.

Faridmehr, I., Osman, M. H., Adnan, A. B., Nejad, A. F., Hodjati, R. & Azimi, M. (2014) Correlation Between Engineering Stress-Strain and True Stress-Strain Curve. *American Journal of Civil Engineering and Architecture.* 2(1), 53-59.

Feigen, M. (1952) Minimum Weight of Tapered Round Thin-Walled Columns. *Journal of Applied Mechanics.* 19(3), 375-380.

Galjaard, S., Hofman, S., Perry, N. & Ren, S. Optimizing Structural Building Elements in Metal by Using Additive Manufacturing. *Proceedings of IASS Annual Symposia, 2015*. International Association for Shell and Spatial Structures (IASS), pp.1-12.

Gao, W., Zhang, Y., Ramanujan, D., Ramani, K., Chen, Y., Williams, C. B., Wang, C. C., Shin, Y. C., Zhang, S. & Zavattieri, P. D. (2015) the Status, Challenges, and Future of Additive Manufacturing in Engineering. *Computer-Aided Design.* 69(12), 65-89.

Gardner, L., Kyvelou, P., Herbert, G. & Buchanan, C. (2020) Testing and Initial Verification of the World's First Metal 3D Printed Bridge. *Journal of constructional steel research.* 172(9), 106233.

Gardner, L. & Nethercot, D. A. (2011) *Designers' Guide to Eurocode 3: Design of Steel Buildings*. London, ICE publishing.

Gatewood, B. (1954) Buckling Loads for Columns of Variable Cross Section. *Journal of the Aeronautical Sciences.* 21(4), 287-288.

Hosain, M. & Spiers, W. (1970) *Experiments on castellated steel beams.* Saskatoon, University of Saskatchewan.

Kanyilmaz, A., Demir, A. G., Chierici, M., Berto, F., Gardner, L., Kandukuri, S. Y., Kassabian, P., Kinoshita, T., Laurenti, A. & Paoletti, I. (2021) Role of Metal 3D Printing To Increase Quality and Resource-Efficiency in the Construction Sector. *Additive Manufacturing.* 50(2), 102541.

Keller, J. B. (1960) The Shape of the Strongest Column. *Archive for Rational Mechanics and Analysis.* 5(1), 275-285.

Laghi, V., Palermo, M., Gasparini, G. & Trombetti, T. (2020) Computational Design and Manufacturing of a Half-Scaled 3D-Printed Stainless Steel Diagrid Column. *Additive Manufacturing.* 36(12), 101505.

Lagrange, J. L. (1770) Sur la figure des colonnes. *Miscellanea Taurinensia.* 5, 123-166.

Malik Chua, J. (2017) *World's First 3D-Printed Pedestrian Bridge Pops Up in Madrid*. https://inhabitat.com/worlds-first-3d-printed-pedestrian-bridge-pops-up-in-madrid/ [Accessed 13th August 2022]

Manickarajah, D., Xie, Y. & Steven, G. (2000) Optimisation of Columns and Frames Against Buckling. *Computers & Structures.* 75(1), 45-54.

Manriquez-Frayre, J. & Bourell, D. Selective Laser Sintering of Binary Metallic Powder. *1990 International Solid Freeform Fabrication Symposium, 1990*.

Maxwell, J. C. (1870) On Reciprocal Figures, Frames, and Diagrams of Forces. *Earth and Environmental Science Transactions of the Royal Society of Edinburgh.* 26(1), 1-40.

Michell, A. G. M. (1904) The Limits of Economy of Material in Frame Structure. *Philosophical Magazine.* 8(6), 589-597.

Moore, N. E. (1996) The Design and Fabrication of a High Temperature Vacuum Workstation for SLS Research. Master thesis. University of Texas at Austin.

Nakagawa, T., Kunieda, M. & Liu, S. Laser Cut Sheet Laminated Forming Dies by Diffusion Bonding. *Proceedings of the 25th International MTDR Conference, 1985*. pp.505-510.

Patel, A. & Desai, C. K. (2020) Stress Concentration Around an Elliptical Hole in a Large Rectangular Plate Subjected to Linearly Varying in-Plane Loading On Two Opposite Edges. *Theoretical and Applied Fracture Mechanics.* 106(4), 102432.

Phair, M. (2004) Rapid Prototyping: the Next Wave in Architectural Modelling. *Building Design & Construction.* 45(11), 15-16.

Pierce, D. & Chou, S. (1973) Stresses Around Elliptic Holes in Circular Cylindrical Shells. *Experimental Mechanics.* 13(11), 487-492.

Sokolowski, J. & Zochowski, A. (1999) On the Topological Derivative in Shape Optimization. *SIAM journal on control and optimization.* 37(4), 1251-1272.

Sonck, D. & Belis, J. (2016) Weak-Axis Flexural Buckling of Cellular and Castellated Columns. *Journal of Constructional Steel Research.* 124(9), 91-100.

Strauss, H., AG, E. P. P. & Knaack, U. (2015) Additive Manufacturing for Future Facades: the Potential of 3D Printed Parts for the Building Envelope. *Journal of Facade Design and Engineering.* 3(3-4), 225-235.

Stromberg, L. L., Beghini, A., Baker, W. F. & Paulino, G. H. (2012) Topology Optimization for Braced Frames: Combining Continuum and Beam/Column Elements. *Engineering Structures.* 37(4), 106-124.

Sweedan, A. M., El-Sawy, K. M. & Martini, M. I. (2009) Identification of the buckling capacity of axially loaded cellular columns. *Thin-Walled Structures.* 47(4), 442-454.

Tadjbakhsh, I. & Keller, J. (1962) Strongest Columns and Isoperimetric Inequalities for Eigenvalues. *Journal of Applied Mechanics.* 29(1), 159-164.

The MathWorks, Inc. (2022). *MATLAB and Curve Fitting Toolbox*. (Version R2022a) [Software] Natick, Massachusetts, United States. The MathWorks, Inc. https://www.mathworks.com.

Thompson, M. K., Moroni, G., Vaneker, T., Fadel, G., Campbell, R. I., Gibson, I., Bernard, A., Schulz, J., Graf, P. & Ahuja, B. (2016) Design for Additive Manufacturing: Trends, Opportunities, Considerations, and Constraints. *CIRP Annals.* 65(2), 737-760.

Timoshenko, S. (1936) *Theory of Elastic Stability*. New York, McGraw-Hill Book Company, Inc.

Trahair, N. & Booker, J. (1970) Optimum Elastic Columns. *International Journal of Mechanical Sciences.* 12(11), 973-983.

Tsavdaridis, K. D., Kingman, J. J. & Toropov, V. V. (2015) Application of Structural Topology Optimisation to Perforated Steel Beams. *Computers & structures.* 158(10), 108-123.

Tuezney, S., Lauwens, K., Afshan, S. & Rossi, B. (2021) Buckling of Stainless Steel Welded I-Section Columns. *Engineering Structures.* 236(6), 111815.

Von Kármán, T. (1932) Strength of thin plates in compression. *Transactions of the ASME.* 54, 53-57.

Wang, M. Y., Wang, X. & Guo, D. (2003) A Level Set Method for Structural Topology Optimization. *Computer methods in applied mechanics and engineering.* 192(1-2), 227-246.

Winsun, W. (2016) Demonstrating the Viability of 3D Printing at Construction Scale. *World Economic Forum, 2016*.

Wong, K. V. & Hernandez, A. (2012) A Review of Additive Manufacturing. *International scholarly research notices.* 2012(8), 208760.

Xie, Y. M. & Steven, G. P. (1993) A Simple Evolutionary Procedure for Structural Optimization. *Computers & structures.* 49(5), 885-896.

Ye, J., Kyvelou, P., Gilardi, F., Lu, H., Gilbert, M. & Gardner, L. (2021) An End-To-End Framework for the Additive Manufacture of Optimized Tubular Structures. *IEEE Access.* 9, 165476-165489.

Yun, X. & Gardner, L. (2017) Stress-Strain Curves for Hot-Rolled Steels. *Journal of Constructional Steel Research.* 133(6), 36-46.

Appendices

A.1 Mesh sensitivity analysis

In this research, the mesh sensitivity analysis was conducted based on the constant height ratio opening models, in which the mesh size of 1.0 mm, 2.0 mm, 4.0 mm and 8.0 mm were investigated. Considering that the minimum dimension of cross-bracing is 3.5 mm, large mesh size will create distorted element layout in bracing which introduces significant inaccuracy. The issue is more pronounced in models with tapered openings. The following **Figure A.1.1** presents the mesh patterns in 3.5 mm cross-bracing tapered opening model, with the element size of 1.0 mm, 2.0 mm, 4.0 mm and 8.0 mm.

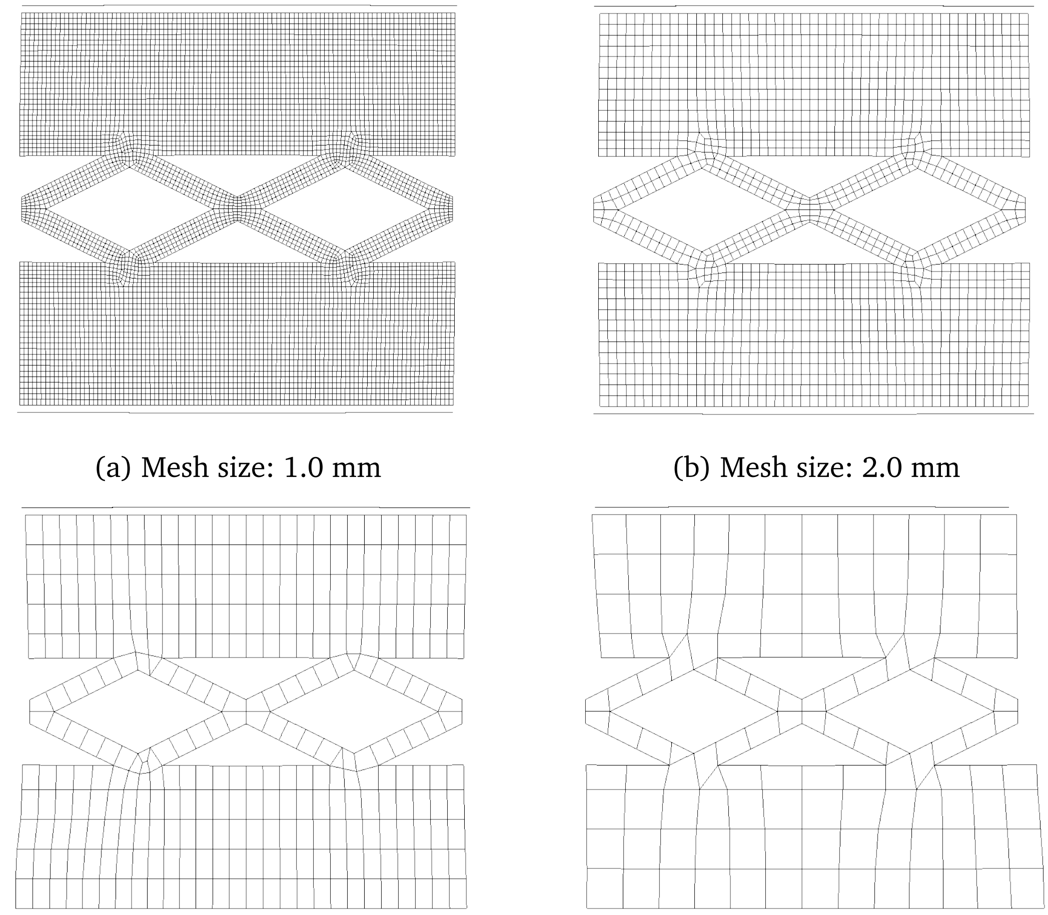

(a) Mesh size: 1.0 mm (b) Mesh size: 2.0 mm

(c) Mesh size: 4.0 mm (d) Mesh size: 8.0 mm

Figure A.1.1: General mesh layouts for a 3.5 mm bracing model (cut section shown for clarity)

Hence, to obtain a reasonable element layout and improve the accuracy in FE results, the mesh sensitivity analysis with consistent web size (1.0 mm) and varying flange mesh size was conducted as well. The mesh size and number of nodes involved in this study are summarised in **Table A.1.1**.

Table A.1.1: Different mesh sizes investigated

Index	Mesh size in web (mm)	Mesh size in flanges (mm)	Number of nodes
1	1.0	1.0	239330
2	2.0	2.0	61561
3	4.0	4.0	16832
4	8.0	8.0	4736
5	1.0	1.0	239330
6	1.0	2.0	147790
7	1.0	4.0	124542
8	1.0	8.0	118516

Based on the mesh combinations mentioned above, the LBA and GMNIA were performed and the results of maximum resistance are plotted in **Figure A.1.2** below.

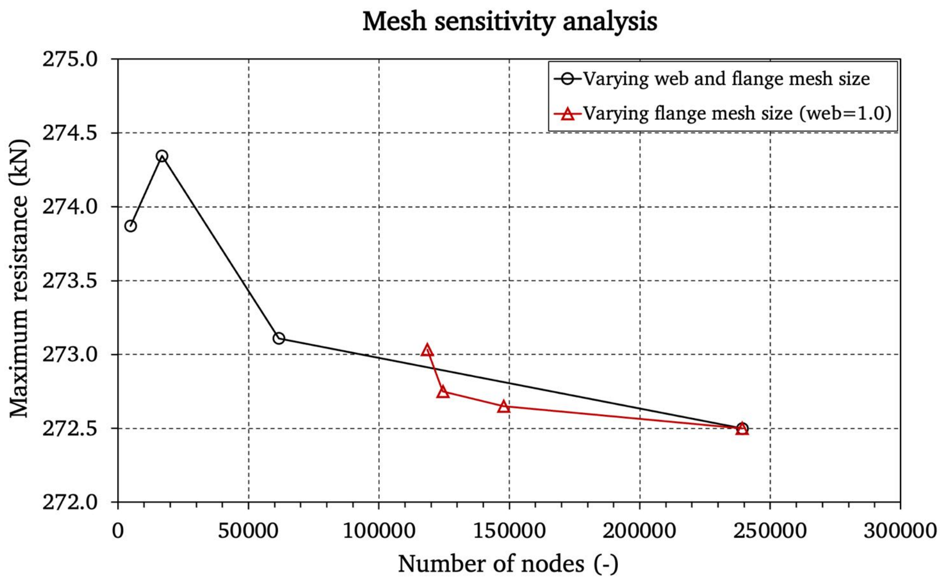

Figure A.1.2: Results of mesh sensitivity study (model: 0.5-0.3-50-3.5)

According to **Figure A.1.2**, with the increasing of number of nodes, the maximum resistances converge towards 272.5 kN. The increments in mesh sizes lead to stiffer structural responses, where result from 8.0 mm mesh model deviates from the predicted trend due to the distorted element layout in bracings. Moreover, with identical web element size (1.0 mm), the levels of resistance do not vary much among the models with 1.0 mm, 2.0 mm and 4.0 mm flange mesh. The surge in resistance of model with 8.0 mm flange mesh might be attributed to the significant element size difference in web and flanges, where the poor interaction issue might arise. Hence, the final mesh size determined is 1.0 mm for web and 4.0 mm for flanges.